Spherical coupled-cluster theory for open-shell nuclei

G. R. Jansen[1, *]

[1]*Department of Physics and Center of Mathematics for Applications, University of Oslo, N-0316 Oslo, Norway*
(Dated: 23rd May 2012)

Background A microscopic description of nuclei is important to understand the nuclear shell-model from fundamental principles. This cannot be achieved without an effective approximation scheme, especially if three-nucleon forces are included.

Purpose Define and evaluate an approximation scheme that can be used to study nuclei that are described as two particles attached to a closed (sub-)shell nucleus.

Methods The equation-of-motion coupled-cluster formalism has been used to obtain ground and excited state energies. This method is based on the diagonalization of a non-Hermitian matrix obtained from a similarity transformation of the many-body nuclear Hamiltonian. A chiral interaction at the next-to-next-to-next-to leading order (N^3LO) using a cutoff at 500 MeV was used.

Results The ground state energies of ^{6}Li and ^{6}He were in good agreement with a no-core shell-model calculation using the same interaction. Several excited states were also produced with overall good agreement. Only the $J^\pi = 3^+$ excited state in ^{6}Li showed a sizeable deviation. The ground state energies of ^{18}O, ^{18}F and ^{18}Ne were converged, but underbound compared to experiment. Also the calculated spectra was converged and comparable to both experiment and shell-model studies in this region. Some excited states in ^{18}O were high or missing in the spectrum.

Conclusions Converged results were obtained for all nuclei and the method can be used to describe nuclear states with simple structure. Especially the ground state energies were very close to an exact diagonalization. To obtain a closer match with experimental data, effects of three-nucleon forces, the scattering contiuum as well as additional configuratons in the coupled-cluster approximations, are necessary.

I. INTRODUCTION

In the past decade, the amount of computing resources made available for scientific research, has grown several orders of magnitude. This trend will continue during this decade, culminating in exascale computing facilities. This will promote new insights in every discipline as new problems can be solved and old problems can be solved faster and to a higher precision.

In nuclear physics, the long standing goal of a predictive theory, seems to approach fulfillment ever faster. However, complex obstacles have yet to be overcome. An exact solution to the nuclear many-body problem, is only possible for light nuclei (See Leidemann and Orlandini [1] for a recent review on many-body methods). With a finite basis expansion, a full diagonalization can currently be performed for nuclei in the p-shell region [2], with the possibilty of approaching light sd-shell nuclei with sufficient computing resources. For *ab initio* access to larger nuclei, the problem has to be approached differently.

In coupled-cluster theory, a series of controlled approximations are performed to generate a similarity transformation of the nuclear Hamiltonian, where the ground state energy of a closed (sub-) shell reference nucleus is singled out. The similarity transformed Hamiltonian is then diagonalized to calculate excited states and states of nuclei with one or more valence nucleons, defining the equation-of-motion coupled-cluster (called EOM-CC

from now on) framework (see Bartlett and Musiał [3] for a recent review and Shavitt and Bartlett [4] for a textbook presentation).

Recently, this method was applied to the oxygen [5] and the calcium [6] isotopic chains, extending the reach of *ab initio* methods in the medium mass region. Calculations in the nickel and tin regions are also planned.

In this work, we refine the EOM-CC method for two valence nucleons attached to a closed (sub-) shell reference. The general theory was presented in Jansen et al. [7], where calculations were performed in small model spaces. The working equations are now completely reworked in the spherical formalism, where the spherical nature of all operators involved, is exploited to its full potential. This involves a fair bit of angular momentum algebra, where the potential for errors is quite large. We therefore explicitly include all equations and transformations for future reference.

Section II gives a brief overview of general coupled-cluster theory and the equation-of-motion extensions, emphasizing the parts that are necessary to develop the spherical scheme presented in Section III. In Section IV we discuss numerical results obtained for selected states in $A = 6$ and $A = 18$ systems, emphasizing the convergence properties. Finally, in Section V we present our conclusions and discuss the road ahead. We also include an appendix, where angular momentum transformations used in Section III are defined.

*Electronic address: g.r.jansen@fys.uio.no

II. COUPLED-CLUSTER THEORY

In this section we introduce the Hamiltonian that enters our calculation, a brief review of single reference coupled cluster-theory together with the equation-of-motion (EOM-CC) extension to coupled cluster theory that allows the calculation of excited states. In this framework, also nuclei with different particle numbers can be approached by choosing the appropriate Slater determinant basis. We keep the presentation short and concentrate on the aspects important for deriving the spherical version of the 2PA-EOM-CCSD method presented in section III. The interested reader is referred to Shavitt and Bartlett [4] for details on coupled-cluster theory.

We use the intrinsic Hamiltonian

$$\hat{H} = \left(1 - \frac{1}{A^*}\right) \sum_{i=1}^A \frac{p_i^2}{2m} + \left[\sum_{i<j=1}^A \hat{v}_{ij} - \frac{\vec{p}_i \cdot \vec{p}_j}{mA^*}\right] . \quad (1)$$

Here A is the number of nucleons in the reference state, A^* is the mass number of the target nucleus, and $\hat{v}_{ij}$ is the nucleon-nucleon interaction. We will limit ourselves to two-body interactions only. In second quantization, the Hamiltonian can be written as

$$\hat{H} = \sum_{pq} \varepsilon_q^p a_p^\dagger a_q + \frac{1}{4} \sum_{pqrs} \langle pq||rs\rangle a_p^\dagger a_q^\dagger a_s a_r . \quad (2)$$

The term $\langle pq||rs\rangle$ is a shorthand for the matrix elements (integrals) of the two-body part of the Hamiltonian of Eq. (1), p, q, r and s represent various single-particle states while ε_q^p stands for the matrix elements of the one-body operator in Eq. (1). Finally, second quantized operators like $a_q^\dagger$ and a_p create and annihilate a nucleon in the state q and p, respectively. These operators fulfill the canonical anti-commutation relations.

A. Single-reference coupled-cluster theory

In single-reference coupled-cluster theory, the many-body ground-state $|\Psi_0\rangle$ is given by the exponential ansatz,

$$|\Psi_0\rangle = \exp\left(\hat{T}\right)|\Phi_0\rangle . \quad (3)$$

Here, $|\Phi_0\rangle$ is the reference Slater determinant, where all states below the Fermi level are occupied and $\hat{T}$ is the cluster operator that generates correlations. The operator $\hat{T}$ is expanded as a linear combination of particle-hole excitation operators

$$\hat{T} = \hat{T}_1 + \hat{T}_2 + \ldots + \hat{T}_A \quad (4)$$

where $\hat{T}_n$ is the n-particle-n-hole(nP-nH) excitation operator

$$\hat{T}_n = \left(\frac{1}{n!}\right)^2 \sum_{a_\nu i_\nu} t_{i_1\ldots i_n}^{a_1\ldots a_n} a_{a_1}^\dagger \ldots a_{a_n}^\dagger a_{i_n} \ldots a_{i_1} . \quad (5)$$

Throughout this work we will use the convention that the indices $ijk\ldots$ denote states below the Fermi level (holes), while the indices $abc\ldots$ denote states above the Fermi level (particles). For an unspecified state, the indices $pqr\ldots$ are used. The amplitudes $t_{i_1\ldots i_n}^{a_1\ldots a_n}$ will be determined by solving the coupled-cluster equations. In the singles and doubles approximation we truncate the cluster operator as

$$\hat{T} \approx \hat{T}_{\text{CCSD}} \equiv \hat{T}_1 + \hat{T}_2 , \quad (6)$$

which defines the coupled-cluster approach with singles and doubles excitations, the so-called CCSD approximation. The unknown amplitudes result from the solution of the non-linear CCSD equations given by

$$\begin{aligned}\langle\Phi_i^a|\bar{H}|\Phi_0\rangle &= 0, \\ \langle\Phi_{ij}^{ab}|\bar{H}|\Phi_0\rangle &= 0 .\end{aligned} \quad (7)$$

The term

$$\bar{H} = \exp\left(-\hat{T}\right)\hat{H}\exp\left(\hat{T}\right) = \left(\hat{H}\exp\left(\hat{T}\right)\right)_C, \quad (8)$$

is called the similarity transform of the normal-ordered Hamiltonian, but (8) only defines a proper similarity transformation when the cluster operator (4) is used without truncation. The state $|\Phi_{ij\ldots}^{ab\ldots}\rangle$ is a Slater determinant that differs from the reference $|\Phi_0\rangle$ by holes in the orbitals $ij\ldots$ and by particles in the orbitals $ab\ldots$. The subscript C indicates that only connected diagrams enter.

Once the t_i^a and t_{ij}^{ab} amplitudes have been determined from Eq. (7), the correlated ground-state energy is given by

$$E_{\text{CC}} = \langle\Phi_0|\bar{H}|\Phi_0\rangle + E_0 . \quad (9)$$

Here, E_0 denotes the vacuum expectation value with respect to the reference state.

The CCSD approximation is a very inexpensive method to obtain the ground state energy of a nucleus. In most cases however, the accuracy is not satisfactory[8]. The obvious solution would be to include triples excitations in Eq. (6) to define the CCSDT approximation. This leads to an additional set of non-linear equations

$$\langle\Phi_{ijk}^{abc}|\bar{H}|\Phi_0\rangle = 0, \quad (10)$$

that has to be solved consistently. Unfortunately, such a calculation is very computationally expensive[9]. The computational cost of CCSDT scales as $n_o^3 n_u^5$, where n_o is the number of single-particle states occupied in the reference determinant and n_u are the number of unoccupied states. For comparison, the computational cost of the CCSD approximation scales as $n_o^2 n_u^4$.

Instead of solving the coupled-cluster equations (7) including triples excitations, we calculate a correction to the correlated ground state energy (9), using the Λ-CCSD(T) approach[10, 11]. Here, the left-eigenvalue problem using the CCSD similarity transformed Hamiltonian is solved, yielding a non-iterative triples correction

to the ground state energy. The left-eigenvalue problem is given by

$$\langle\Phi_0|\hat{\Lambda}\bar{H} = E\langle\Phi_0|\hat{\Lambda}, \tag{11}$$

where $\hat{\Lambda}$ is a de-excitation operator,

$$\hat{\Lambda} = \hat{1} + \hat{\Lambda}_1 + \hat{\Lambda}_2, \tag{12}$$

and

$$\hat{\Lambda}_1 = \sum_{ia} \lambda_a^i a_a a_i^\dagger, \tag{13}$$

$$\hat{\Lambda}_2 = \sum_{ijab} \lambda_{ab}^{ij} a_b a_a a_i^\dagger a_j^\dagger. \tag{14}$$

The unknown amplitudes λ_a^i and λ_{ab}^{ij} are the components of the left-eigenvector with the lowest eigenvalue in Eq. (11). Once found, the energy correction is given by

$$\Delta E_3 = \frac{1}{(3!)^2} \sum_{ijkabc} \langle\Phi_0|\hat{\Lambda}\left(\hat{F}_{hp} + \hat{V}_N\right)|\Phi_{ijk}^{abc}\rangle$$
$$\times \frac{1}{\epsilon_{ijk}^{abc}}\langle\Phi_{ijk}^{abc}|\left(\hat{V}_N\hat{T}_2\right)_C|\Phi_0\rangle. \tag{15}$$

Here, $\hat{F}_{hp}$ is the part of the normal-ordered one-body Hamiltonian that annihilates particles and creates holes. The energy denominator is defined as

$$\epsilon_{ijk}^{abc} \equiv f_{ii} + f_{jj} + f_{kk} - f_{aa} - f_{bb} - f_{cc}, \tag{16}$$

where f_{pp} are the diagonal elements of the normal ordered one-body Hamiltonian $\hat{F}$.

Using this approach, the ground state wave function (3) and the similarity transformed Hamiltonian (8) are calculated using the CCSD approximation, while the ground state energy is given by

$$E_{\Lambda CC} = E_{CC} + \Delta E_3 \tag{17}$$

This approximation has proven to give very accurate results for closed (sub-)shell nuclei[12].

B. Equation-of-motion coupled-cluster(EOM-CC)

In nuclear physics, the single reference coupled cluster method defined by the coupled-cluster equations(7), is normally used to obtain the ground state energy of a closed (sub-)shell nucleus. While it is possible to apply the CC method to any reference determinant to obtain the energy of different states, the equation-of-motion coupled-cluster (EOM-CC) framework is usually employed for such endeavors.

When the cluster operator (4) is used without truncation, Eq. (8) defines a similarity transformation. This guarantees that the eigenvalues of $\bar{H}$ are equivalent to the eigenvalues of the intrinsic Hamiltonian (1) and that the eigenvectors are connected by the transformation defined by Eq. (3). When the cluster operator (4) is truncated, as in the CCSD approximation, Eq. (8) is an approximation to a similarity transformation. This means that the eigenvalues of $\bar{H}$ are now only approximations to the exact eigenvalues. This is the foundation of the EOM-CC approach.

To simplify the equations and for effective calculations, we define the eigenvalue problem in the EOM-CC approach to be that of the difference between a target state and the coupled cluster ground state (3). Formally, a general state of the A-body nucleus is written

$$|\Psi_\mu\rangle = \hat{\Omega}_\mu|\Psi_0\rangle = \hat{\Omega}_\mu e^{\hat{T}}|\Phi_0\rangle. \tag{18}$$

Here $\hat{\Omega}_\mu$ is an excitation operator that creates the state $|\Psi_\mu\rangle$, when applied to the coupled cluster ground state $|\Psi_0\rangle$. The label μ identifies the quantum numbers(energy, angular momentum, ...) of the target state. The Schrödinger equations for the target state and the coupled-cluster ground state are written

$$\hat{H}\hat{\Omega}_\mu e^{\hat{T}}|\Phi_0\rangle = E_\mu\hat{\Omega}_\mu e^{\hat{T}}|\Phi_0\rangle \tag{19}$$

$$\hat{H}e^{\hat{T}}|\Phi_0\rangle = E_{CC}e^{\hat{T}}|\Phi_0\rangle. \tag{20}$$

Here E_μ is the energy of the target state and E_{CC} is the coupled-cluster reference energy in Eq. (9).

We can now multiply Eq. (19) by $e^{-\hat{T}}$ and Eq. (20) by $\hat{\Omega}_\mu e^{-\hat{T}}$ from the left and take the difference between the two equations

$$\left[\bar{H}, \hat{\Omega}_\mu\right]|\Psi_0\rangle = \omega_\mu\hat{\Omega}_\mu|\Psi_0\rangle, \tag{21}$$

where $\omega_\mu = E_\mu - E_{CC}$ and we have used that $\left[\hat{\Omega}_\mu, \hat{T}\right] = 0$. Finally, none of the unconnected terms in the evaluation of the commutator survive, resulting in

$$\left(\bar{H}\hat{\Omega}_\mu\right)_C|\Phi_0\rangle = \omega_\mu\hat{\Omega}_\mu|\Phi_0\rangle. \tag{22}$$

This operator equation can be posed as a matrix eigenvalue problem where ω_μ are the eigenvalues and the matrix elements of $\hat{\Omega}_\mu$ are the components of the eigenvectors. The subscript C implies that only terms where $\bar{H}$ and $\hat{\Omega}_\mu$ are connected by at least one contraction survive. In diagrammatic terms, this means that only connected diagrams appear in the operator product $\left(\bar{H}\hat{\Omega}_\mu\right)_C$.

The similarity transformed Hamiltonian (8) is a non-hermitian operator and is diagonalized by the scheme formulated by the Arnoldi algorithm(for details see for example Golub and Van Loan [13]). This scheme relies on the repeated application of the connected matrix vector product defined by Eq. (22). A left-eigenvalue problem is solved to obtain the conjugate eigenvectors[14], but this is beyond the scope of this article.

To find the explicit expressions for the connected matrix vector product, the excitation operator must be properly defined. When used for excited states of an A-body

nucleus, the excitation operator in Eq. (18) is parametrized in terms of nP-nH operators. We define

$$\hat{\Omega}_\mu = \hat{R} = \hat{1} + \hat{R}_1 + \hat{R}_2 + \ldots \hat{R}_A, \qquad (23)$$

where

$$\hat{R}_n = \frac{1}{(n!)^2} \sum_{\substack{i_1,\ldots i_n \\ a_1,\ldots a_n}} r^{a_1\ldots a_n}_{i_1\ldots i_n} a^\dagger_{a_1} \ldots a^\dagger_{a_n} a_{i_n} \ldots a_{i_1}. \qquad (24)$$

The unknown amplitudes r(sub and superscripts dropped) are the matrix elements of $\hat{R}$,

$$r^{a_1\ldots a_n}_{i_1\ldots i_n} = \langle \Phi^{a_1\ldots a_n}_{i_1\ldots i_n} | \hat{R} | \Phi_0 \rangle, \qquad (25)$$

and can be grouped into a vector that solves the eigenvalue problem in Eq. (22). The matrix vector product is found by looking at each individual element

$$\left(\bar{H}\hat{R} \right)^{a_1\ldots a_n}_{i_1\ldots i_n} \equiv \langle \Phi^{a_1\ldots a_n}_{i_1\ldots i_n} | \left(\bar{H}\hat{R} \right)_C | \Phi_0 \rangle, \qquad (26)$$

and find the appropriate expressions using a diagrammatic approach.

Calculations using the full excitation operator (23), are not computationally tractable, so an additional level of approximation is introduced by a truncation. When the CCSD approximation is used to obtain the reference wave function, the excitation operator is truncated at the 2P-2H level[15] and defines EOM-CCSD.

In the EOM-CC approach, the states of $A \pm k$ nuclei are also treated as excited states of an A-body nucleus. We write

$$|\Psi^{A\pm k}_\mu\rangle = \hat{\Omega}_\mu |\Psi^{(A)}_0\rangle = \hat{\Omega}_\mu e^{\hat{T}} |\Phi_0\rangle. \qquad (27)$$

The operator $\hat{\Omega}_\mu$ and the energies E_μ of the target state, also solve the eigenvalue problem in Eq. (22). The energy difference $\omega_\mu = E_\mu - E^*_0$ is now the excitation energy of the target state in the nucleus $A \pm k$, with respects to the closed-shell reference nucleus with the mass shift $A^* = A \pm k$ in the Hamiltonian (1). This mass shift ensures the correct kinetic energy of the center-of-mass is used in computing the $A \pm k$ nuclei.

The operators

$$\hat{\Omega}_\mu = \hat{R}^{A\pm 1} = \hat{R}^{A\pm 1}_1 + \hat{R}^{A\pm 1}_2 + \ldots \hat{R}^{A\pm 1}_A \qquad (28)$$

where

$$\hat{R}^{A+1}_n = \frac{1}{(n!)(n-1)!} \sum_{\substack{i_1,\ldots i_{n-1} \\ a_1,\ldots a_n}} r^{a_1\ldots a_n}_{i_1\ldots i_{n-1}}$$
$$\times a^\dagger_{a_1} \ldots a^\dagger_{a_n} a_{i_{n-1}} \ldots a_{i_1} \qquad (29)$$

$$\hat{R}^{A-1}_n = \frac{1}{(n!)(n-1)!} \sum_{\substack{i_1,\ldots i_n \\ a_1,\ldots a_{n-1}}} r^{a_1\ldots a_{n-1}}_{i_1\ldots i_n}$$
$$\times a^\dagger_{a_1} \ldots a^\dagger_{a_{n-1}} a_{i_n} \ldots a_{i_1} \qquad (30)$$

define the particle attached equation-of-motion coupled-cluster [16] (PA-EOM-CC) and the particle removed equation-of-motion coupled-cluster [17](PR-EOM-CC) approaches. These methods have been used successfully in quantum chemistry for some time (see Bartlett and Musiał [3] for a review), but have also recently been implemented for use in nuclear structure calculations [18].

In Jansen et al. [7] we defined the 2PA-EOM-CCSD and 2PR-EOM-CCSD methods for two particle attached to and removed from a closed (sub-)shell nucleus. For this problem, the excitation operators were given by

$$\hat{\Omega}_\mu = \hat{R}^{A\pm 2} = \hat{R}^{A\pm 2}_2 + \hat{R}^{A\pm 2}_3 + \ldots \hat{R}^{A\pm 2}_A \qquad (31)$$

where

$$\hat{R}^{A+2}_n = \frac{1}{(n!)(n-2)!} \sum_{\substack{i_1,\ldots i_{n-2} \\ a_1,\ldots a_n}} r^{a_1\ldots a_n}_{i_1\ldots i_{n-2}}$$
$$\times a^\dagger_{a_1} \ldots a^\dagger_{a_n} a_{i_{n-2}} \ldots a_{i_1} \qquad (32)$$

$$\hat{R}^{A-2}_n = \frac{1}{(n!)(n-2)!} \sum_{\substack{i_1,\ldots i_n \\ a_1,\ldots a_{n-2}}} r^{a_1\ldots a_{n-2}}_{i_1\ldots i_n}$$
$$\times a^\dagger_{a_1} \ldots a^\dagger_{a_{n-2}} a_{i_n} \ldots a_{i_1}. \qquad (33)$$

In this article, our focus is on the 2PA-EOM-CCSD method, where we truncate the operator at the 3P-1H level. This approximation is suitable for states with a dominant 2P structure. It is already computationally intensive with up to 10^9 basis states for the largest nuclei. A full inclusion of 4P-2H amplitudes is therefore not feasible at this time.

C. Spherical coupled cluster theory

For nuclei with closed (sub)shell structure, the reference state has good spherical symmetry and zero total angular momentum. For these systems, the cluster operator(4) is a scalar under rotation and depends only on reduced amplitudes. Thus,

$$\hat{T}_1 = \sum_{ia} t^a_i(J) \left[a^\dagger_a(J) \otimes \tilde{a}_i(J) \right]^0$$

and

$$\hat{T}_2 = \sum_{ijabJ} t^{ab}_{ij}(J) \left[\left[a^\dagger_a(j_a) \otimes a^\dagger_b(j_b) \right]^J \otimes [\tilde{a}_j(j_j) \otimes \tilde{a}_i(j_i)]^J \right]^0,$$

where the amplitudes $t(J)$(sub- and superscript dropped) are a short form of the reduced matrix elements of the cluster operator (4) (See appendix A for details). Also, J is a label specifying the total angular momentum of a many-body state and standard tensor notation has been used to specify the tensor couplings.

As the similarity transformed Hamiltonian (8) is a product of three scalar operators(remember that the exponential of an operator is defined in terms of its Taylor

expansion), it is also a scalar under rotation. This allows a formulation of the coupled-cluster equations that is completely devoid of magnetic quantum numbers, thus reducing the size of the single particle space and the number of coupled non-linear equations to solve in Eq. (7). For further details, see Hagen et al. [12].

Within the same formalism, we wish to establish the connected operator product in Eq. (22). This will greatly reduce the computational cost of calculating the product, but also allow a major reduction in both the single-particle basis and the number of allowed configurations in the many-body basis.

Given a target state with total angular momentum J (in units of $\hbar c$), the excitation operator, Ω_μ(18), is a spherical tensor operator by definition(see for example Bohr and Mottelson [19]). It has a rank of J, with $2J+1$ components labelled by the magnetic quantum number $M \in [-J, \ldots, J]$. We write

$$\Omega_\mu = \hat{R}_\mu^{A\pm k}(J, M), \qquad (34)$$

where A is the number of particles in the reference state, $A \pm k$ is the number of particles in the target state, while μ identifies a specific set of quantum numbers. Identifying the excitation operator as a spherical tensor operator, invokes an extensive machinery of angular momentum algebra with important theorems. Of special importance is the Wigner-Eckart theorem(see for example Edmunds [20]), which states that the matrix elements of a spherical tensor operator can be factorized into two parts. The first is a geometric part identified by a Clebsch-Gordon coefficient, while the second is a reduced matrix element that does not depend on the magnetic quantum numbers.

To derive the spherical form of any EOM-CCSD method, a suitable spherical many-body basis has to be defined. The Slater determinant basis where we use the particle-hole formalism is substituted with the standard form. That means that for a general operator $\hat{O}$, we will write

$$\langle ab|\hat{O}|ij\rangle \equiv \langle \Phi_{ij}^{ab}|\hat{O}|\Phi_0\rangle, \qquad (35)$$

where the single-particle states labelled a and b are occupied in the outgoing state, while the single-particle states labelled i and j are occupied in the incoming state. All single-particle states shared between the incoming and outgoing many-body state are dropped from the notation.

In general form, we write a component of the spherical basis as

$$|\alpha; J_\alpha M_\alpha\rangle, \qquad (36)$$

where α denotes a particular many-body state, while $J_\alpha(M_\alpha)$ is the total angular momentum(projection) of this state. Using the spherical notation, the matrix elements of the excitation operator are written

$$r_\beta^\alpha(J_\alpha, J_\beta) = \langle \alpha; J_\alpha M_\alpha|\hat{R}_M^J|\beta; J_\beta M_\beta\rangle, \qquad (37)$$

where we have dropped the cumbersome sub- and superscripts on the excitation operator in favour of standard tensor notation. The matrix elements of the matrix vector product in Eq. (22) are written

$$\langle \alpha; J_\alpha M_\alpha| \left(\bar{H}\hat{R}_M^J\right)_C |\beta; J_\beta M_\beta\rangle = \\ \omega\langle \alpha; J_\alpha M_\alpha|\hat{R}_M^J|\beta; J_\beta M_\beta\rangle. \qquad (38)$$

Now, the Wigner-Eckart theorem allows a factorization of the matrix elements into two factors

$$C_{MM_\beta M_\alpha}^{JJ_\beta J_\alpha}\langle \alpha; J_\alpha|| \left(\bar{H}\hat{R}^J\right)_C ||\beta; J_\beta\rangle = \\ \omega C_{MM_\beta M_\alpha}^{JJ_\beta J_\alpha}\langle \alpha; J_\alpha||\hat{R}^J||\beta; J_\beta\rangle. \qquad (39)$$

Here, $C_{MM_\beta M_\alpha}^{JJ_\beta J_\alpha}$ is a Clebsch-Gordon coefficient and the double bars denote reduced matrix elements and does not depend on any of the projection quantum numbers. This equation is simplified by dividing by the Clebsch-Gordon coefficient. This means that for each set of α, β, J_α and J_β, where J, J_α and J_β satisfy the triangular condition, there are $(2J + 1) \times (2J_\alpha + 1) \times (2J_\beta + 1)$ identical equations for a given J. Of course, we only need one to solve the eigenvalue problem, resulting in significantly smaller dimensionality. We are left with an eigenvalue problem where the unknown components of the eigenvectors are the reduced matrix elements of the excitation operator

$$\langle \alpha; J_\alpha|| \left(\bar{H}\hat{R}^J\right)_C ||\beta; J_\beta\rangle = \omega\langle \alpha; J_\alpha||\hat{R}^J||\beta; J_\beta\rangle. \qquad (40)$$

The eigenvalue problem in Eq. (40) is the spherical formulation of the general EOM-CC diagonalization problem. For a given excitation operator, both the connected operator product and the reduced amplitudes must be defined explicitly.

III. DERIVATION OF SPHERICAL 2PA-EOM-CCSD

In this work we derive the spherical formulation of the 2PA-EOM-CCSD [7] method, where the excitation operator in Eq. (31) has been truncated at the 3P-1H level. We write

$$\hat{R} = \frac{1}{2} \sum_{ab} r^{ab} a_a^\dagger a_b^\dagger + \frac{1}{6} \sum_{abci} r_i^{abc} a_a^\dagger a_b^\dagger a_c^\dagger a_i, \qquad (41)$$

where we have dispersed with the cumbersome sub- and subscripts in the operator.

The unknown amplitudes r are the matrix elements of $\hat{R}$ and defined by

$$r^{ab} = \langle \Phi^{ab}|\hat{R}|\Phi_0\rangle \equiv \langle ab|\hat{R}|0\rangle \\ r_i^{abc} = \langle \Phi_i^{abc}|\hat{R}|\Phi_0\rangle \equiv \langle abc|\hat{R}|i\rangle, \qquad (42)$$

while we define a shorthand form of the components of the matrix-vector product by

$$\left(\bar{\mathrm{H}}\hat{\mathrm{R}}\right)^{ab} = \langle\Phi^{ab}|\left(\bar{\mathrm{H}}\hat{\mathrm{R}}\right)_C|\Phi_0\rangle \qquad (43)$$

$$\left(\bar{\mathrm{H}}\hat{\mathrm{R}}\right)_i^{abc} = \langle\Phi_i^{abc}|\left(\bar{\mathrm{H}}\hat{\mathrm{R}}\right)_C|\Phi_0\rangle. \qquad (44)$$

The eigenvalue problem in Eq. (22) can now be posed in terms of the individual equations

$$\left(\bar{\mathrm{H}}\hat{\mathrm{R}}\right)^{ab} = \omega r^{ab}$$
$$\left(\bar{\mathrm{H}}\hat{\mathrm{R}}\right)_i^{abc} = \omega r_i^{abc}. \qquad (45)$$

In the spherical formulation, the excitation operator is a spherical tensor operator of rank J and projection M,

$$\hat{\mathrm{R}}_M^J = \frac{1}{2}\sum_{ab} r^{ab}(J)\left[a_a^\dagger(j_a)\otimes a_b^\dagger(j_b)\right]_M^J$$
$$+ \frac{1}{6}\sum_{\substack{abci\\J_{ab}J_{abc}}} r_i^{abc}\left(J, J_{abc}, J_{ab}\right)$$
$$\times\left[\left[\left[a_a^\dagger(j_a)\otimes a_b^\dagger(j_b)\right]^{J_{ab}}\otimes a_c^\dagger(j_c)\right]^{J_{abc}}\otimes\tilde{a}_i(j_i)\right]_M^J. \qquad (46)$$

Here the $a_a^\dagger(j_a)$ and $\tilde{a}_i(j_i)$ are spherical tensor operators of rank j_a and j_i respectively, where the latter is the time-reversed operator of $a_i^\dagger(j_i)$. Standard tensor notation has been used to define the spherical tensor couplings. The reduced amplitudes are now the reduced matrix elements of the spherical excitation operator (46). We write

$$r^{ab}(J) = \langle ab; j_a j_b; J||\hat{\mathrm{R}}^J||0\rangle, \qquad (47)$$

where j_a and j_b are coupled to J in left to right order. Also

$$r_i^{abc}\left(J, J_{abc}, J_{ab}\right) = \langle abc; j_a j_b; J_{ab}j_c; J_{abc}||\hat{\mathrm{R}}^J||i; j_i\rangle, \qquad (48)$$

where we have coupled the angular momentums j_a and j_b to J_{ab}, as well as J_{ab} and j_c to J_{abc}, also in left to right order. The shorthand form of the reduced matrix elements of the connected operator product is defined analogously by

$$\left(\bar{\mathrm{H}}\hat{\mathrm{R}}^J\right)^{ab}(J) = \langle ab; j_a j_b; J||\left(\bar{\mathrm{H}}\hat{\mathrm{R}}^J\right)_C||0\rangle \qquad (49)$$

and

$$\left(\bar{\mathrm{H}}\hat{\mathrm{R}}^J\right)_i^{abc}(J, J_{abc}, J_{ab}) =$$
$$\langle abc; j_a j_b; J_{ab}j_c; J_{abc}||\left(\bar{\mathrm{H}}\hat{\mathrm{R}}^J\right)_C||i; j_i\rangle. \qquad (50)$$

The transformations that connect the reduced matrix elements of $\hat{\mathrm{R}}^J$ with the uncoupled matrix elements are given in Eqs. (A16)-(A19).

The spherical eigenvalue problem (40) can now be written

$$\left(\bar{\mathrm{H}}\hat{\mathrm{R}}^J\right)^{ab}(J) = \omega r^{ab}(J)$$
$$\left(\bar{\mathrm{H}}\hat{\mathrm{R}}^J\right)_i^{abc}(J, J_{abc}, J_{ab}) = \omega r_i^{abc}(J, J_{abc}, J_{ab}), \qquad (51)$$

where the amplitudes are now the reduced matrix elements defined above.

In Table I we list the main result of this section. The first column lists all possible diagrams that contribute to the matrix-vector product in Eqs. (45), and (51). The other two columns contain the closed form expressions for these diagrams, in both the uncoupled and in the spherical representation. All matrix elements and amplitudes are defined in appendix A, while the permutation operators $\hat{\mathrm{P}}(a,b)$ and $\hat{\mathrm{P}}(ab,c)$ are defined in appendix B. Note that in the spherical representation the permutation operators also change the coupling order.

The last two diagrams contain the three-body parts of the similarity transformed Hamiltonian (8) and have been joined in the spherical representation. The details of this merger and the definition of the intermediate operator $\hat{\chi}$ are contained in appendix C.

Let us briefly discuss how we arrive at the spherical diagram expressions, where we will use the first diagram in Table I as an example. This diagram contributes to the 2P matrix elements defined in Eq. (43) in the uncoupled representation and to the reduced matrix elements defined in Eq. (49) in the spherical representation.

The first step is to use the transformation in Eq. (A16) to write the reduced matrix elements (49) in terms of the uncoupled matrix elements (43). This gives us

$$\left(\bar{\mathrm{H}}\hat{\mathrm{R}}^J\right)^{ab}(J) = \frac{1}{\hat{J}^2}\sum_{Mm_a m_b} C_{m_a m_b M}^{j_a j_b J}\left(\bar{\mathrm{H}}\hat{\mathrm{R}}\right)^{ab}, \qquad (52)$$

where we introduce the notation $\hat{J} = \sqrt{2J+1}$. The diagram contributions to the uncoupled matrix elements are given by

$$\left(\bar{\mathrm{H}}\hat{\mathrm{R}}\right)^{ab} \leftarrow \hat{\mathrm{P}}(ab)\bar{\mathrm{H}}_e^b r^{ae}, \qquad (53)$$

where we let the arrow indicate that this is only one of several contributions to this matrix element. Here, $\bar{\mathrm{H}}_e^b$ is a matrix element of the one-body part of the similarity transformed Hamiltonian (8) and both $\bar{\mathrm{H}}_e^b$ and r^{ae} are in the uncoupled representation.

Second, we insert Eq. (53) into Eq. (52) and get

$$\left(\bar{\mathrm{H}}\hat{\mathrm{R}}\right)^{ab}(J) \leftarrow \frac{1}{\hat{J}^2}\sum_{Mm_a m_b} C_{m_a m_b M}^{j_a j_b J}\bar{\mathrm{H}}_e^b r^{ae} \qquad (54)$$

Note that for the moment, we have ignored the permutation operator $\hat{\mathrm{P}}(ab)$ that is a part of the diagram. We will discuss this later.

Diagram	Uncoupled expression	Coupled expression
	$\hat{P}(ab)\bar{H}_e^b r^{ae}$	$\hat{P}(ab)\bar{H}_e^b(j_b)r^{ae}(J)$
	$\frac{1}{2}\bar{H}_{ef}^{ab}r^{ef}$	$\frac{1}{2}\bar{H}_{ef}^{ab}(J)r^{ef}(J)$
	$\bar{H}_e^m r_m^{abe}$	$\sum_{J_{abe}}\bar{H}_e^m(j_e)r_m^{abe}(J_{ab},J_{abe},J)\frac{\hat{J}_{abe}^2}{\hat{J}^2}$
	$\frac{1}{2}\hat{P}(ab)\bar{H}_{ef}^{bm}r_m^{aef}$	$\frac{1}{2}\hat{P}(ab)\sum_{J_{efb},J_{ef}}(-1)^{1+j_b+j_m-J_{ef}-J}\frac{\hat{J}_{efb}^2\hat{J}_{ef}}{\hat{J}}\begin{Bmatrix} j_b & j_a & J \\ j_m & J_{efb} & J_{ef}\end{Bmatrix}$ $\times\bar{H}_{ef}^{am}(J_{ef})r_m^{efb}(J_{ef},J_{efb},J)$
	$\hat{P}(a,bc)\bar{H}_{ei}^{bc}r^{ae}$	$\hat{P}(ab,c)(-1)^{1+j_c+j_i+J_{ab}-J}\hat{J}_{ab}\hat{J}\begin{Bmatrix} j_c & j_e & J \\ j_i & J_{abc} & J_{ab}\end{Bmatrix}\bar{H}_{ab}^{ei}(J_{ab}r^{ec}(J)$
	$\hat{P}(ab,c)\bar{H}_e^c r_i^{abe}$	$\hat{P}(ab,c)\bar{H}_e^c(j_c)r_i^{abe}(J_{ab},J_{abe},J)$
	$-\bar{H}_i^m r_m^{abc}$	$-\bar{H}_m^i(j_i)r_m^{abc}(J_{ab},J_{abc},J)$
	$\frac{1}{2}\hat{P}(ab,c)\bar{H}_{ef}^{ab}r_i^{efc}$	$\frac{1}{2}\hat{P}(ab,c)\bar{H}_{ef}^{ab}(J_{ab})r_i^{efc}(J_{ab},J_{abc},J)$
	$\hat{P}(ab,c)\bar{H}_{ei}^{mc}r_m^{abe}$	$\hat{P}(ab,c)\sum_{J_{abe},J_{mc}}(-1)^{1+j_e+j_m+J_{abe}+J_{abc}+J_{mc}}\hat{J}_{abe}^2\hat{J}_{mc}^2\begin{Bmatrix} J_{ab} & j_e & J_{abe} \\ j_c & J_{mc} & j_m \\ J_{abc} & j_i & J\end{Bmatrix}$ $\times\bar{H}_{ei}^{mc}(J_{mc})r_m^{abe}(J_{ab},J_{abe},J)$
	$\frac{1}{2}\bar{H}_{efi}^{abc}r^{ef}$	$(-1)^{1+j_c+j_m-J}\hat{J}\hat{J}_{ab}\begin{Bmatrix} j_c & j_m & J \\ j_i & J_{abc} & J_{ab}\end{Bmatrix}\chi_m^c(J)t_{im}^{ab}(J_{ab})$
	$\frac{1}{2}\hat{P}(a,bc)\bar{H}_{efi}^{bmc}r_m^{aef}$	

Table I: All diagrams for the 2PA-EOM-CCSD method with both ordinary and reduced amplitudes and matrix elements. The reduced amplitudes and matrix elements are defined in appendix A, while $\chi_i^a(J)$ is defined in appendix C. Note that the two last diagrams are combined into one expression in the spherical formulation and that repeated indices are summed over.

Third, we use the reverse transformations in Eqs. (A11) and (A17) to transform the uncoupled matrix elements of $\bar{H}_e^b$ and r^{ae} to the corresponding reduced matrix elements. This gives us

$$\left(\bar{H}\hat{R}\right)^{ab}(J) \leftarrow \frac{1}{\hat{J}^2}\sum_M \bar{H}_e^b(j_b)r^{ae}(J)$$
$$\times \sum_{m_a m_b}\delta_{j_b,j_e}\delta_{m_b,m_e}C_{m_a m_b M}^{j_a j_b J}C_{m_a m_e M}^{j_a j_e J}, \quad (55)$$

where δ is the Kronecker delta and results from the application of the Wigner-Eckart theorem to the matrix element of $\bar{H}$. Orthogonality of the Clebsch-Gordon coefficients gives

$$\sum_{m_a m_b}\delta_{j_b,j_e}\delta_{m_b,m_e}C_{m_a m_b M}^{j_a j_b J}C_{m_a m_e M}^{j_a j_e J} = 1, \quad (56)$$

and we are left with

$$\left(\bar{H}\hat{R}\right)^{ab}(J) \leftarrow \bar{H}_e^b(j_b)r^{ae}(J). \quad (57)$$

Note that $\sum_M 1 = 2J+1$ and that repeated indices are summed over.

Initially, we left out the permutation operator $\hat{P}(a,b)$ that is needed to generate antisymmetric amplitudes. In the uncoupled representation this operator is defined as

$$\hat{P}(ab) = \hat{1} - \hat{P}_{a,b}, \quad (58)$$

where $\hat{1}$ is the identity operator and $\hat{P}_{a,b}$ changes the order of the two indices a and b, but leaves the coupling order unchanged. Let us apply this operator to $\left(\bar{H}\hat{R}\right)^{ab}(J)$. The result is

$$\hat{P}(a,b)\left(\bar{H}\hat{R}\right)^{ab}(J) =$$
$$\left(\bar{H}\hat{R}\right)^{ab}(J) - \langle ba; j_a j_b; J||\left(\bar{H}\hat{R}\right)_C ||0\rangle, \quad (59)$$

where the last matrix element has the wrong coupling order compared to the reduced amplitudes defined in Eq. (49) where

$$\left(\bar{H}\hat{R}\right)^{ba}(J) = \langle ba; j_b j_a; J||\left(\bar{H}\hat{R}\right)_C ||0\rangle. \quad (60)$$

To change the coupling order, we exploit the symmetry properties of the Clebsch-Gordon coefficients and write

$$\langle ba; j_a j_b; J||\left(\bar{H}\hat{R}\right)_C ||0\rangle =$$
$$(-1)^{j_a+j_b-J}\langle ba; j_b j_a; J||\left(\bar{H}\hat{R}\right)_C ||0\rangle$$
$$= (-1)^{j_a+j_b-J}\left(\bar{H}\hat{R}\right)^{ba}(J). \quad (61)$$

As a consequence of this, we define the permutation operator in the spherical representation to also change the coupling order. This results in the following definition

$$\hat{P}(ab) = \hat{1} - (-1)^{j_a+j_b-J}\hat{P}_{a,b}. \quad (62)$$

The total contribution from the first diagram in Table I in the spherical representation is

$$\left(\bar{H}\hat{R}\right)^{ab}(J) \leftarrow \hat{P}(ab)\bar{H}^b_e(j_b)r^{ae}(J), \quad (63)$$

where $\hat{P}(ab)$ is defined by Eq. (62).

We define the more complicated three-body permutation operators $\hat{P}(ab,c)$ in the same manner, but they must change the coupling order of three angular momentums. The details have been left to appendix B.

IV. RESULTS

A. Model space and interaction

All calculations in this section have been done in a spherical Hartree-Fock basis, based on harmonic oscillator single particle wave functions. These are identified with the set of quantum numbers $\{nlj\}$ for both protons and neutrons, where n represents the number of nodes, l represents the orbital momentum, and finally j is the total angular momentum of the single particle wave function.

We will identify the size of the model space by the variable

$$N_{\max} = \max(N), \quad (64)$$

where $N = 2n + l$, so that the number of harmonic oscillator shells is $N_{\max} + 1$. All single particle states with

$$2n + l \leq N_{\max}$$

are included and no additional restrictions are made on the allowed configurations. Thus, $N_{\max}$ completely determines the computational size and complexity of the calculations.

$N_{\max}$	Size	Elements	Memory
10	132	145 623 788	1.1 Gb
12	182	587 531 302	4.4 Gb
14	240	1 963 734 704	14.6 Gb
16	306	5 687 352 954	42.4 Gb
18	380	14 715 230 212	109 Gb
20	458	33 622 665 364	250 Gb

Table II: The first column contains the size of the single particle basis employed for different model spaces labelled by $N_{\max}$(See text for details). Column two and three list the number of matrix elements for the different model spaces and the memory footprint of the interaction in our implementation. All numbers are based on the coupled representation, also known as the jj-scheme basis.

In Table II we list the size of the single particle space for different values of $N_{\max}$. In addition, the table includes the total number of matrix elements defining the interaction in Eq. (1), as well as the memory footprint in our calculations. Given the memory requirements alone, it is clear that a distributed storage scheme is needed from the beginning.

In addition to the interaction elements, we also need to store the Arnoldi vectors in the diagonalization procedure. Typically 150 iterations are performed, where one vector has to be stored for each iteration. Table III lists the size of a single EOM vector for selected target states for various model spaces. For a double precision calculation, where each element requires 8 bytes of storage, the Arnoldi diagonalization would require $\approx$ 76Gb of memory for a calculation of the $J^\pi = 3^+$ state of ^{6}Li with $N_{\max} = 16$. Thus the Arnoldi procedure quickly becomes the largest memory consumer in this method. In general, there is a steep performance penalty in increasing the total angular momentum of the target state, which is comparable to increasing the size of the model space.

Our interaction is derived from chiral perturbation theory at next-to-next-to-next-to-leading order(N^{3}LO) using interaction matrix elements of Entem and Machleidt [21]. The matrix elements of this interaction employs a cutoff $\Lambda = 500$ MeV and all partial waves up to relative

State	$N_{\max} = 10$	$N_{\max} = 12$	$N_{\max} = 14$	$N_{\max} = 16$	$N_{\max} = 18$	$N_{\max} = 20$
^{6}He(0^+)	516 048	1 323 972	2 981 930	6 088 376	11 513 088	20 176 104
^{6}He(1^-)	1 507 930	3 894 028	8 808 688	18 040 354	34 190 482	60 011 982
^{6}He(2^+)	2 391 692	6 251 128	14 255 896	29 364 090	55 885 624	98 356 664
^{6}Li(0^+)	775 992	1 989 508	4 478 936	9 142 216	17 284 308	30 285 212
^{6}Li(1^+)	2 268 746	5 853 534	13 234 004	27 093 632	51 335 514	90 080 136
^{6}Li(2^+)	3 595 384	9 391 650	21 409 878	44 088 456	83 893 672	147 629 532
^{6}Li(3^+)	4 676 372	12 438 258	28 699 916	59 604 726	114 125 048	201 657 602
^{18}O(0^+)	1 908 474	5 022 710	11 485 808	23 680 034	45 071 990	79 331 610
^{18}O(1^-)	5 594 899	14 802 528	33 974 801	70 231 288	133 940 727	236 049 974
^{18}O(2^+)	8 891 923	23 794 936	55 036 119	114 391 274	219 038 683	387 077 788
^{18}O(2^-)	8 897 760	23 803 219	55 047 530	114 406 595	219 058 796	387 083 193
^{18}O(3^+)	11 613 562	31 596 862	73 906 056	154 840 950	298 237 942	529 098 382
^{18}O(3^-)	11 621 868	31 608 838	73 922 708	154 863 424	298 267 524	529 107 862
^{18}O(4^+)	13 629 562	37 905 214	89 982 332	190 504 054	369 757 342	659 327 780
^{18}F(0^+)	2 868 568	7 545 420	17 248 686	35 552 756	67 658 660	119 071 548
^{18}F(1^+)	8 403 602	22 228 738	51 009 366	105 427 688	201 040 066	354 285 892
^{18}F(2^+)	13 362 878	35 742 012	82 642 970	171 734 254	328 788 766	580 957 010
^{18}F(3^+)	17 451 568	47 458 334	110 973 350	232 452 890	447 659 068	794 095 862
^{18}F(4^+)	20 479 376	56 930 198	135 106 850	285 982 274	554 996 372	989 530 134
^{18}F(5^+)	22 363 324	63 896 228	154 444 460	331 158 558	648 765 300	1 163 943 530

Table III: Size of the many-body space in the diagonalization procedure in the Arnoldi algorithm for all states calculated in this work. All numbers are based on the coupled representation, also known as the jj-scheme basis.

angular momentum $J_{rel} = 6$ are included. We do not include relevant three- and four-body interactions defined by the chiral expansion at this order.

When we discuss the center-of-mass contamination of the final solution, we will also need a softer interaction where the short range parts are removed via the similarity renormalization group transformation[22]. We will use a cutoff $\lambda = 2.0\text{fm}^{-1}$ for this purpose.

B. Center of mass contamination

Recently, Hagen et al. [23] showed that the coupled-cluster wave function separates into an intrinsic part and a Gaussian for the center-of-mass coordinate. This means that we do not have to worry about the center-of-mass contamination of physical states, as the results will converge to a separated solution.

In the EOM-CC approach we make further approximations by truncating the many-body basis before the diagonalization is performed. It is therefore not clear that the final wave functions separates in the same way as the coupled-cluster reference state.

Following the procedure in Hagen et al. [23], we calculated the expectation value of the center-of-mass energy at the proper frequency, for the ground state of ^{6}He, the first excited $J^\pi = 1^-$ state in ^{6}He and the first excited $J^\pi = 3^+$ state in ^{6}Li. The calculations were performed in a model space defined by $N_{\max} = 14$, with an SRG interaction with a momentum cutoff at $\lambda = 2.0 \text{ fm}^{-1}$.
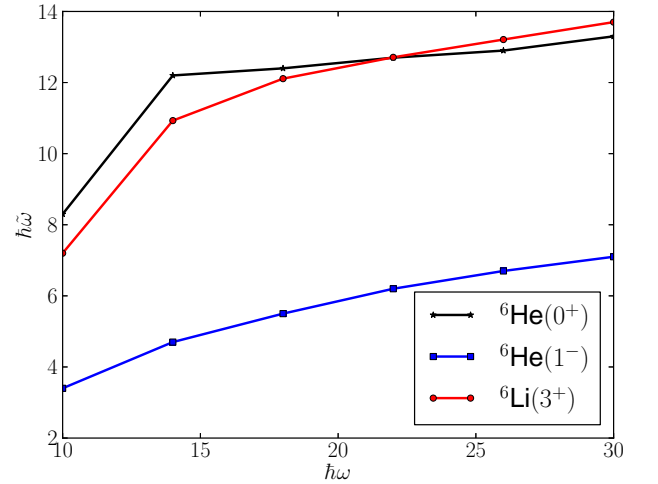

Figure 1: Center-of-mass frequency as calculated by the description in Hagen et al. [23] as a function of the oscillator parameter $\hbar\omega$. Three different states are shown – the $J^\pi = 0+$ ground state of ^{6}He, the $J^\pi = 1^-$ excited state in ^{6}He and the $J^\pi = 3^+$ excited state in ^{6}Li.

Fig. 1 shows the calculated center-of-mass frequency as a function of the oscillator parameter $\hbar\omega$ defining the single particle basis, while Fig. 2 shows the center-of-mass energy at this new frequency.

Immediately, two things are evident. First, the $J^\pi = 1^-$ state in ^{6}He does not separate. The center-of-mass energy is very high and we conclude that this state is

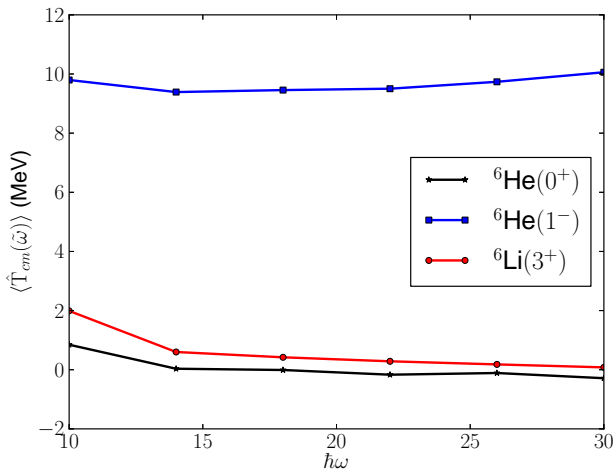Figure 2: The expectation value of the center-of-mass energy is calculated at the center-of-mass frequency $\hbar\bar{\omega}$ for the $J^\pi =$ 0+ ground state of ^{6}He, the $J^\pi = 1^-$ excited state in ^{6}He and the $J^\pi = 3^+$ excited state in ^{6}Li.

unphysical. There are no documented $J^\pi = 1^-$ low-lying states in the ^{6}He spectrum. Second, the ground state of ^{6}He separates, as the center-of-mass energy is approximately zero. At low frequencies, the calculation is not quite converged, yielding a higher center-of-mass admixture in the wave function.

Let us comment further on the $J^\pi = 3^+$ state in ^{6}Li. Here, the center-of-mass energy is not quite zero, although very close at approximately 300 keV. This is a physical state, as ^{6}Li has this state low in its spectrum. It must be said that the Hellman-Feynmann theorem used to calculate these values is not exact, so small errors can occur. In addition, the calculation might not be fully converged, but we saw no significant changes between calculations done at $N_{\max} = 12$ and $N_{\max} = 14$. Finally, it can be that the result is not converged with respect to the truncations made in the theory. If this is the case, it might be possible to use the center-of-mass contamination as a measure of convergence. We will touch upon this subject in the next two sections, but a detailed analysis is left to future work.

C. Applications to ^{6}Li and ^{6}He

For any given reference nucleus, there are only three nuclei accessible to the 2PA-EOM-CC method. Using ^{4}He as the reference, we can add two protons to calculate properties of ^{6}Be, two neutrons for ^{6}He and finally a proton and a neutron to calculate properties of ^{6}Li. Of these, only ^{6}Li and ^{6}He are stable with respect to nucleon emission and we will only concentrate our efforts on these. Looking at the structure of ^{6}Li and ^{6}He, they are very different. This is an important point, because the quality of the current level of approximation will inevitably depend on the structure of the nucleus.

^{6}Li is well bound and has four bound states below the nucleon emission threshold at 4.433 MeV[24]. The ground state has spin parity assignment $J^\pi = 1^+$, while the first excited states have $J^\pi = 3^+$, 2^+ and 0^+. The $J^\pi = 0^+$ ground state in ^{6}He is a two neutron halo state, bound by only 800 keV[24] compared to ^{4}He. There are no bound excited states – only a narrow resonance at 1.710 MeV is documented[24].

First we discuss convergence with respect to the size of the model space. Our approach is based on a finite basis expansion, where $N_{\max}$ effectively determines the numerical cutoff. We increase the cutoff until the corrections are so small that the uncertainties in our calculation outweighs these differences.
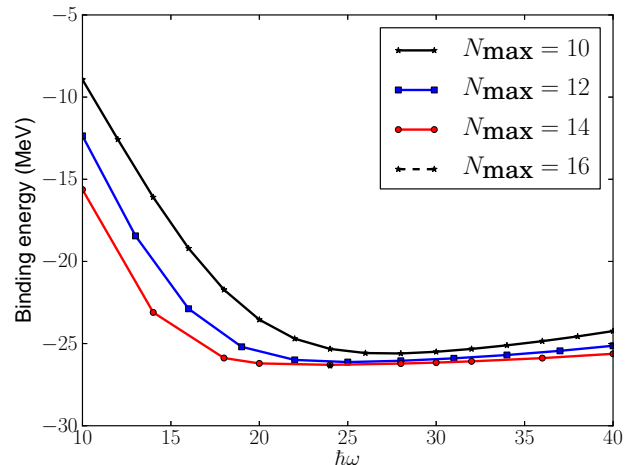

Figure 3: Ground state energy of ^{6}Li as a function of the oscillator parameter $\hbar\omega$ and the size of the model space $N_{\max}$(see text for details).

Fig. 3 shows the calculated total binding energy of ^{6}Li, as a function of the oscillator frequency $\hbar\omega$. Different lines correspond to different model spaces. At $N_{\max} = 16$, there is a shallow minimum around $\hbar\omega = 24$ MeV and in a 10 MeV range including this minimum, the binding energy varies by approximately 100 keV. This is less than half a percent of the total energy. At low frequencies, the energy deviates substantially from the minimum, due to the lack of resolution in the single particle space.

Note that the gain in binding energy when going from $N_{\max} = 14$ to $N_{\max} = 16$ is also very small, about 40 keV. We conclude that the binding energy of ^{6}Li is converged with respect to the size of the model space ($N_{\max}$). The energy at $\hbar\omega = 24$ MeV will be our tabulated result.

The picture is largely identical for the binding energy of ^{6}He, only the minimum in energy occurs at $\hbar\omega = 20$ MeV. Here the difference in energy between the two largest model space is about 140 keV.

To show that the excited states follow the same pattern of convergence as the ground state, in Fig. 4 we plot the total energy of the $J^\pi = 3^+$ state in ^{6}Li. As before, the energy is plotted as a function of $\hbar\omega$ and different lines correspond to different values of $N_{\max}$. Our estimation
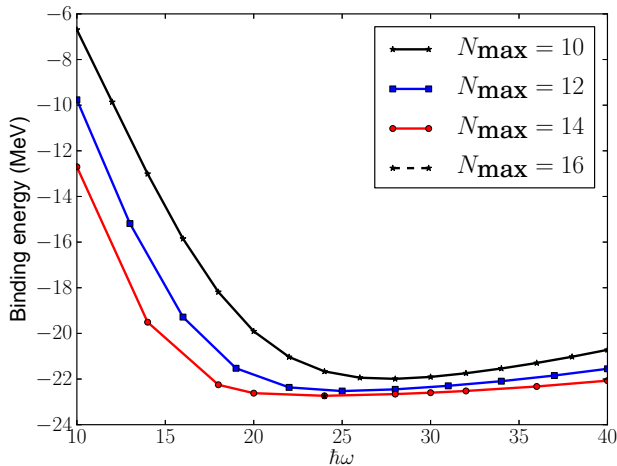
Figure 4: The total energy of the first excited $J^\pi = 3^+$ state of ^{6}Li as a function of the oscillator parameter $\hbar\omega$ and the size of the model space $N_{\max}$(see text for details).

of excitation energies will also be taken at specific values of $\hbar\omega$, where we simply take the difference in energy to the ground state at the minimum value. For the calculation of excitation energies in this section, this causes no concern as the minima in energies for all excited states are located at the same $\hbar\omega$ value as the minima for the ground states. (See next section for a discussion of cases where this is not correct.)
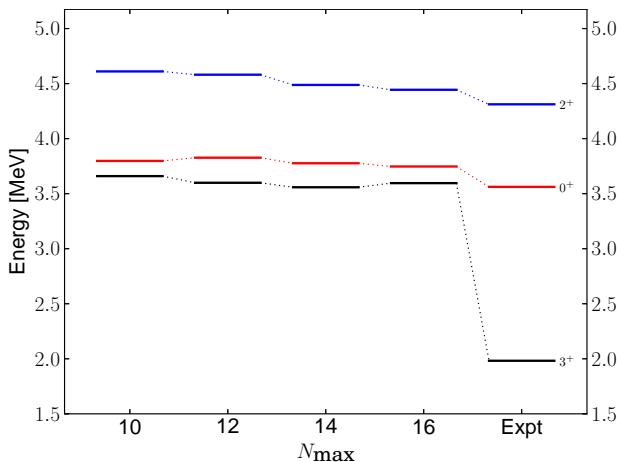

Figure 5: Excitation energy for selected states of ^{6}Li, as a function of the size of the model space defined by $N_{\max}$. The rightmost column shows the experimental values from Tilley et al. [24].

In Fig. 5 we show the convergence of the excitation energies for selected states in the spectrum of ^{6}Li. The horizontal axis denotes the size of the model space, where the rightmost column are the experimental values [24]. All excitation energies have been calculated at $\hbar\omega = 24$ MeV, which correspond to the minimum of the ground state energy. All three states show very little dependence on the size of the model space at $N_{\max} = 16$. None of the states

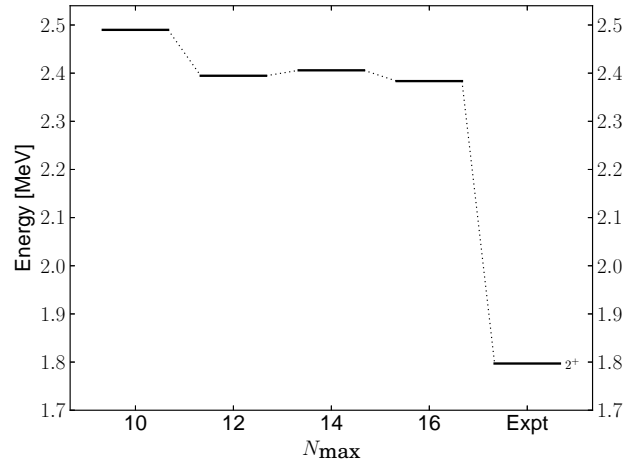Figure 6: Excitation energy for the first excited $J^\pi = 2^+$ state of of ^{6}He, as a function of the size of the model space defined by $N_{\max}$. The rightmost column shows the experimental value from Tilley et al. [24].

show any significant center-of-mass contamination, so we conclude that they are converged. We also found an additional $J^\pi = 1^+$ state higher in the spectrum, but this state had a large center-of-mass admixture in the wave function and are therefore not included.

In Fig. 6 we show an equivalent plot for the first $J^\pi = 2^+$ excited state in ^{6}He, which is also converged with respect to the size of the model space. No significant center-of-mass contamination was found neither in this state nor the ground state, but this was not the case for the $J^\pi = 1^-$ state, as already discussed. Note that the scale of the vertical axis of this plot is significantly smaller than that of Fig. 5 and that all excitation energies for ^{6}He were calculated at $\hbar\omega = 20$ MeV.

We also look at some properties of the wave function. Although it is not an observable, other expectation values might be more sensitive to changes in the wave function than the energy. For this purpose we define two properties. First, the partial norms are defined by

$$n(2p0h) = \sum_{ab}(2J + 1)\left(r^{ab}(J)\right)^2 \qquad (65)$$

$$n(3p1h) = \sum_{\substack{abci \\ J_{ab}J_{abc}}} (2J_{abc} + 1)\left(r_i^{abc}(J_{ab}, J_{abc}, J)\right)^2, \quad (66)$$

where $n(2p0h) + n(3p1h) = 1$. The amplitudes $r^{ab}(J)$ and $r_i^{abc}(J_{ab}, J_{abc}, J)$ are the spherical amplitudes defined in Eqs. (A16) and (A18) respectively, while J_x are angular momentum labels. Note that the angular momentum factors are included so that the partial norms are consistent between the coupled and uncoupled scheme. These norms quantify the part of the wave function in 2P-0H and 3P-1H configurations respectively.

Second, we define the total weights

$$w_{pw}^{ab} = (2J + 1)\sum_{a,b}\left[\left(r_{pw}^{ab}(J)\right)^2 + \left(r_{pw}^{ba}(J)\right)^2\right], \quad (67)$$

where the label pw identifies the partial wave content of the weight. The sum is over all configurations with this partial wave content, because the weights of individual configurations are not stable. Only at high frequencies do single configurations dominate. The total weights however, are reasonably stable already at this level.

State	$n(2p0h)$	Dominant configuration(s)	Weight(s)
^{6}Li(1_1^+)	0.77	$(\pi p_{3/2}\nu p_{1/2})$, $(p_{3/2})^2$	0.40, 0.30
^{6}Li(3^+)	0.76	$(p_{3/2})^2$	0.67
^{6}Li(0^+)	0.72	$(p_{3/2})^2$, $(p_{1/2})^2$	0.60, 0.11
^{6}Li(2_1^+)	0.77	$(\pi p_{3/2}\nu p_{1/2})$	0.640
^{6}He(0^+)	0.71	$(p_{3/2})^2$, $(p_{1/2})^2$	0.59, 0.11
^{6}He(2^+)	0.74	$(p_{3/2})^2$, $(p_{3/2}p_{1/2})$	0.47, 0.25
^{6}He(1^-)	0.65	$(s_{1/2}p_{3/2})$, $(d_{5/2}p_{3/2})$	0.32, 0.18

Table IV: This table shows the 2P-0H partial norms (65), as well as the dominant configurations for calculated states in both ^{6}Li and ^{6}He. The weights are calculated according to Eq. (67) where all nodes for a given partial wave contribute to the sum. The numbers in parenthesis are the differences of the maximum and minimum values for $\hbar\omega = 20 - 40$ and indicate the level of convergence of the wave function.

We list the partial norms and dominant weights of selected states in ^{6}Li and ^{6}He in Table IV. The ground state of ^{6}Li is dominated by configurations that have a proton in the $p_{3/2}$ orbital and a neutron in the $p_{1/2}$ or the $p_{3/2}$ orbitals. Note that both partial norms and the total weights are more sensitive to changes in the model space than the energy and that the weights are becoming more unstable approaching the nucleon emission threshold. Again the $J^\pi = 1^-$ stands out with a low 2P-0H content. The 2P-0H structure of all the physical states in this table conform with the shell model picture of two nucleons in the p-shell, but all states have an additional 3P-1H content that cannot be neglected. Additional refinements of our method using also 4P-2H configurations are necessary to analyze this further.

In Table V we show results with estimated numerical uncertainties for the ground and selected excited states of both ^{6}He and ^{6}Li. For comparison, both experimental values and results from a no-core shell-model (NCSM) calculation [25] are tabulated where data is available. Note that the results from the NCSM calculation are based on the same interaction as the results from this work, but the interaction is renormalized using the procedure defined in Suzuki and Lee [26], before the diagonalization was performed. In addition, the final results were extrapolated to an infinite model space.

Let us discuss the uncertainties indicated by the parenthesis in the table. For the results from this work, listed in the second column, the numbers in parenthesis simple give the difference in energy between the two largest model spaces. The results from Navrátil and Caurier [25] give the extrapolation errors in the last column, while the experimental energies [24] in the first column are listed without uncertainties.

Fig. 7 shows a graphical representation of the data in Table V. Compared to the results from the NCSM

^{6}Li	Expt.	N^{3}LO ($\Lambda = 500$MeV)	NCSM[25]
$E_{gs}(1^+)$	-31.993	$-28.44(5)$	$-28.5(5)$
$E_{gs}(1^+)$	0.0	0.0	0.0
$E_x(3_1^+)$	$+2.186$	$+3.60(4)$	$+2.91(3)$
$E_x(0_1^+)$	$+3.562$	$+3.76(3)$	$+3.30(10)$
$E_x(2_1^+)$	$+4.312$	$+4.44(4)$	$+4.10(15)$
^{6}He			
$E_{gs}(0^+)$	-29.270	$-25.51(14)$	$-26.2(5)$
$E_{gs}(0^+)$	0.0	0.0	0.0
$E_x(2^+)$	1.797	2.35(4)	

Table V: Binding energies and excitation energies for selected states of ^{6}Li and ^{6}He with estimated numerical uncertainties. The uncertainties in our results are the differences between the values for the two largest model spaces. The data is compared to NCSM results [25] in the rightmost column, where the parenthesis list extrapolation errors and experimental data in the leftmost column. All experimental data are from Tilley et al. [24].
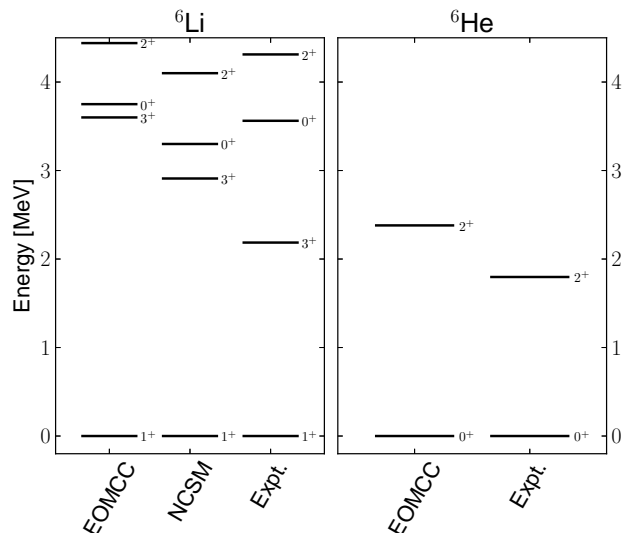

Figure 7: Excitation levels of selected states in ^{6}Li and ^{6}He, calculated using 2PA-EOM-CC(this work) and NCSM [25], while compared to experimental [24] values.

calculation, our results are quite promising. First, the ground state energy of ^{6}Li is well within the uncertainties of the "exact" result, while the ground state energy of ^{6}He is just outside. The difference between the two nuclei can be explained by the extended spatial distribution of ^{6}He. Additional correlations are necessary to account for this structure. Although the alpha core in ^{6}He is expected to stay largely unchanged when adding two neutrons, the distribution of these extra neutrons are biased in one direction. This results in a skewed center-of-mass compared to the center-of-mass of the alpha core alone. Additional correlations are necessary to absorb the resulting oscillations of the alpha core with respect

to the combined center-of-mass. The spatial distribution of ^{6}Li is tighter, so this effect is not that prominent in this nucleus. Second, the ordering of excited states in ^{6}Li is reproduced.

We do however, consistently overestimate the excitation energies. While the difference for the first $J^\pi = 0^+$ and 2^+ states are small enough to be attributed to the difference between the calculations, this is not so for the $J^\pi = 3^+$ state. Our results differ by about 700 keV for this state. Neither the partial norms nor the total weights listed in Table IV provide any hint of explanation for this discrepancy. About 76 percent of the wave function is in 2P-0H configurations, which is comparable to the ground state. The wave function is dominated by configurations where both nucleons are in $p_{3/2}$ orbitals, which is consistent with the shell-model picture. Furthermore, the level of convergence for this state is no different from the other excited states. We do however, find a slight center-of-mass admixture in the wave function of the $J^\pi = 3^+$ state, which is not present in the other states. This was illustrated in Fig. 2, where we used a softer renormalized interaction. Now, the calculated center-of-mass contamination is too small to be conclusive, especially since the calculation is only approximate and the analysis has been performed using a softer renormalized interaction. We include it because it might indicate that additional correlations are needed in the calculation, either in the reference or the EOM operator. This matter needs to be investigated further, but currently the implementation will not allow model spaces large enough for a converged description of the center-of-mass admixture in the final wave function.

Using the in-medium similarity renormalization group (IM-SRG), Tsukiyama et al. [27] performed a similar study with a softer interaction. Here, the $J^\pi = 3^+$ state in ^{6}Li is reproduced on the same level of accuracy as the other bound states. We therefore conclude that the discrepancy in our result is due to the approximations done in 2PA-EOM-CCSD.

Let us also comment on the differences between our results and the experimental values. First, we see that all excitation energies are overestimated compared to data. Again, the $J^\pi = 3^+$ states is exceptional, but this has been discussed in detail by Navrátil and Caurier [25]. The matter was resolved by the inclusion of three-nucleon forces [28], which also brought the binding energy very close to data.

For the $J^\pi = 2^+$ resonance in ^{6}He, this seems not to be the case. We also calculated this state using a chiral interaction with a different cutoff of 600 MeV and found the excitation energy of this state to be largely cutoff dependent. This was not so for the excited states in ^{6}Li, where especially the $J^\pi = 3^+$ state turned out to be very cutoff dependent. We can better explain the discrepancy in energy of the resonance in ^{6}He, by missing continuum degrees of freedom. The current single particle basis cannot handle the description of both bound, resonance and continuum states necessary in this case. While we are

working on the inclusion of the Gamow shell-model [29] in the 2PA-EOM-CC method, as has been done for coupled-cluster in Hagen et al. [30] a discussion of this is beyond the scope of this article.

Summing up this section, we conclude that for well bound states, with simple structure, the current approximation will yield total energies comparable to exact diagonalization. For weakly bound states, continuum degrees of freedom are necessary for a quantitative comparison to exact results. In addition, we find that we are able to reach sufficiently large model-spaces for our results to be converged for six nucleons, but for certain states, especially the $J^\pi = 3^+$ state in ^{6}Li, the effects of 4P-2H configurations need to be investigated.

D. Applications to ^{18}O and ^{18}F

When ^{16}O is used as a reference state, the three isobars ^{18}O, ^{18}F and ^{18}Ne are reachable by the 2PA-EOM-CC method. All have well bound ground states and a rich spectra of bound excited states below their respective nucleon emission thresholds. The spectrum of ^{18}F is especially rich, as the exclusion principle do not affect the placement of nucleons in the sd-shell. The proton-neutron interaction is responsible for the compressed spectrum in the fluorine isotope, while strong pairing effects in ^{18}O and ^{18}Ne results in lower ground state energies. In both ^{18}O and ^{18}Ne the spectra is opened up and the first excited states are higher in energy. Our current focus is on convergence and the viability of this method. Thus, ^{18}Ne is not explicitly discussed, as results are similar to that of ^{18}O.
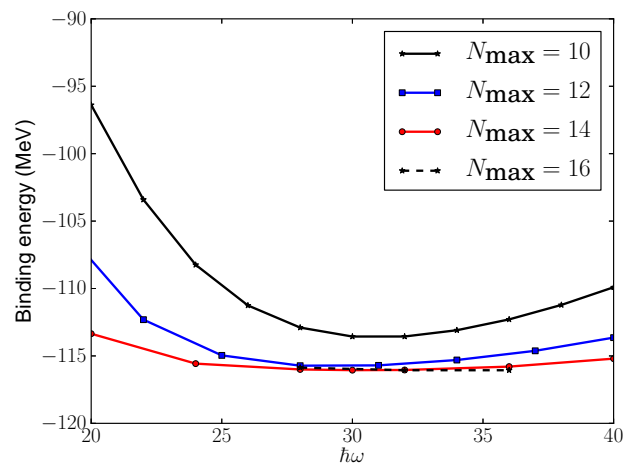

Figure 8: The ground state energy of ^{18}O as a function of the oscillator parameter, $\hbar\omega$. Different lines correspond to different model spaces, parametrized by the variable $N_{\max}$ (64).

Let us first look at the convergence of the binding energy of ^{18}O. In Fig. 8, we plot the ground state energy of ^{18}O as a function of the oscillator parameter $\hbar\omega$. The different lines correspond to different model spaces, para-

metrized by the variable N_{max} (64). A shallow minimum develops around $\hbar\omega = 32$ MeV, where the energy is converged with respect to the size of the model space. The difference in energy is about 20 keV when the size of the model space is increased from $N_{max} = 14$ to $N_{max} = 16$. We also see that for a wide range of values around the minimum, the ground state energy shows very little dependence on the $\hbar\omega$ parameter. This state is exceptionally well converged and is a testament to the bound nature of this state.

A similar result is obtained for the ground state energy of ^{18}F, where the difference in energy is around 160keV between the two largest model spaces. This is almost an order of magnitude larger than for the ground state of ^{18}O, but is still well within one percent of the total energy.
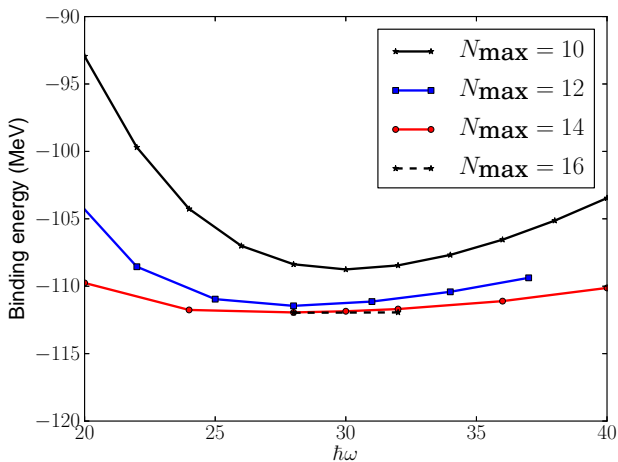

Figure 9: The total energy of the $J^\pi = 3+$ state in ^{18}O as a function of the oscillator parameter, $\hbar\omega$. Different lines correspond to different model spaces, parametrized by the variable N_{max} (64).

In Fig. 9 we plot the total energy of the first excited $J^\pi = 3^+$ state in ^{18}O for different model spaces. Here we see a shallow minimum develop at $\hbar\omega = 28$ MeV. Also this state is very well converged, with a difference in energy of only about 25 keV between calculations in the two largest model spaces. We clearly see that the rate of convergence is different for different values of $\hbar\omega$. This will be an issue when we want to calculate excitation energies, as different choices of $\hbar\omega$ lead to different results. To evaluate the excitation energy, we highlight two options. We can treat the total energies as variational results and choose the lowest energy for the ground state and the lowest energy for the $J^\pi = 3^+$ excited state. Thus, at $N_{max} = 16$ we calculate the excitation energy as

$$E_x(3^+) = E_{3^+}(28\text{MeV}) - E_{0_1^+}(32\text{MeV}), \qquad (68)$$

where $E_{3^+}(28\text{MeV})$ is the total energy of the $J^\pi = 3^+$ excited state, calculated at $\hbar\omega = 28$ MeV, while $E_{0_1^+}(32\text{MeV})$, is the ground state energy calculated at $\hbar\omega = 32$ MeV.

The second option is to use the same value of $\hbar\omega$ for both energies, where we choose the value where the ground state has a minimum. Thus, for the current case we calculate the excitation energy as

$$E_x(3^+) = E_{3^+}(32\text{MeV}) - E_{0_1^+}(32\text{MeV}). \qquad (69)$$

The difference in energy between these two options is minimal if sufficiently large model spaces is used, but it will have a significant impact on the rate of convergence.
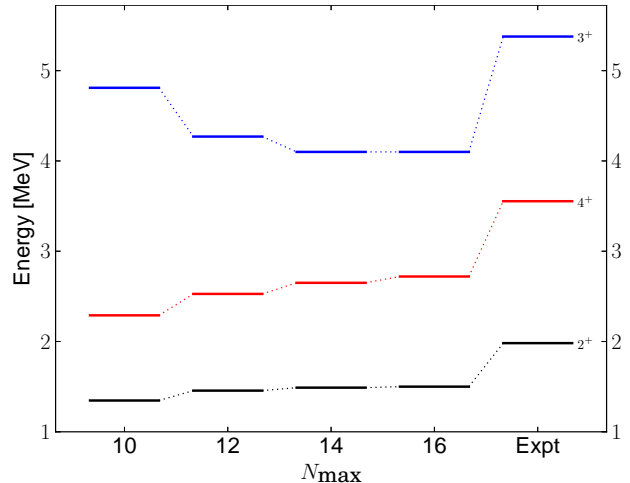

Figure 10: The excitation energies of the first $J^\pi = 2^+$, 3^+ and 4^+ excited states in ^{18}O where the best values for $\hbar\omega$ has been chosen for each state. The different columns represents different model spaces parametrized by the variable N_{max} (64). The rightmost column contains experimental values from Tilley et al. [31].

Figure 11: The excitation energies of the first $J^\pi = 2^+$, 3^+ and 4^+ excited states in ^{18}O for $\hbar\omega = 32$ MeV. The different columns represents different model spaces parametrized by the variable N_{max} (64). The rightmost column contains experimental values from Tilley et al. [31].
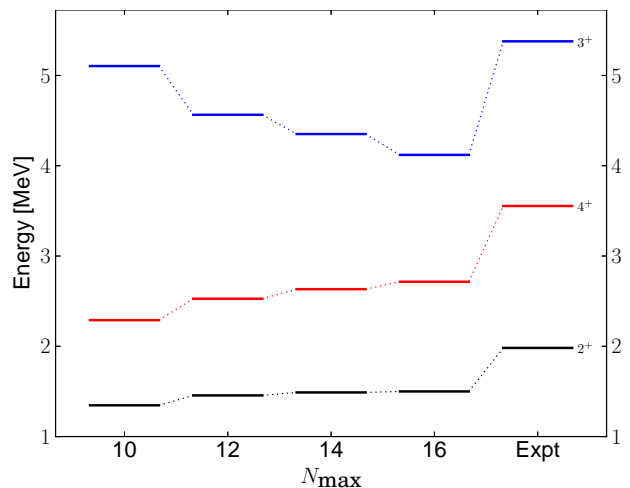
The effect is best viewed in Figs. 10 and 11, where we plot the excitation energy of the first $J^\pi = 2^+$, 3^+ and 4^+

excited states in ^{18}O as functions of the size of the model space. In Fig. 10, the excitation energy is calculated according to Eq. (68), while it is calculated according to Eq. (69) in Fig. 11. For ^{18}O, this choice will only affect the $J^\pi = 3^+$ state, as the other states all have minimum values at $\hbar\omega = 32$ MeV. The effect is significant, but we feel the first approach of Fig. 10 correctly depictis the level of convergence of the excited states. All three states in this plot are very well converged, but the $J^\pi = 4^+$ state displays a slightly larger model space dependence than the other two states.

To further evaluate these states, we look at some of the properties of the wave function. First, we checked that the wave function separates approximately into an intrinsic part and a center-of-mass part, following the recipe outlined in Hagen et al. [23]. None of these states showed any center-of-mass contamination. Second, we looked at the partial norm defined in Eq. (65) and also the relative weights of the different configurations in the final wave function. In Table VI we list these properties for all states calculated in this section.

The $J^\pi = 2^+$ and 4^+ states are dominated by configurations where two neutrons are in the $d_{5/2}$ orbital, but as can be seen in Table VI, the $J^\pi = 2^+$ state shows significant admixture of configurations where one neutron is in the $d_{5/2}$ orbital while the other is in the $s_{1/2}$ orbital. The $J^\pi = 3^+$ state is dominated by the latter configuration. Thus, all three states conform with the shell-model picture of two neutrons in the sd-shell outside an ^{16}O core. They also show the same level of 2P-0H content – around 70 percent.

In contrast, we can look at the three negative parity states that show up in the ^{18}O spectrum. First, from Table VI we see that the 2P-0H content of the wave functions are significantly lower for the negative parity states.

Second, Fig. 12 shows that the excitation energies of these states are not converged at $N_{max} = 16$, and far from experimental data. Finally, the center-of-mass contamination of all three states is rather large and similar to the $J^\pi = 1^-$ state in ^{6}He (see Fig. 2). We must therefore conclude that the current truncation is not sufficient to reproduce these states. It will be necessary to include 4P-2H correlations to get the negative parity states right. We can understand this by examining how negative parity states can be produced in ^{18}O. First, it can be produced by placing one neutron in the sd-shell, while the other is placed in the pf-shell. If this was the dominant configuration, the current truncation would have been enough. Secondly, it can also be produced by placing two neutrons in the sd-shell and excite nucleons from the p-shell up to the sd-shell. If this excitation is comparable in energy to the first configuration, 3P-1H configurations start to dominate and 4P-2H configurations are probably necessary.

As a side note, we also see that the wave function of these negative parity states are spread over a large number of configurations with significant contributions from
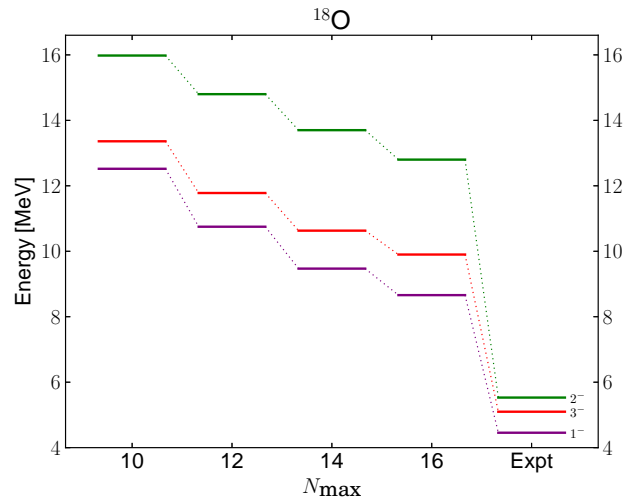
higher partial waves.

In the spectrum of ^{18}O, there are three bound $J^\pi = 0^+$ and 2^+ states. The second $J^\pi = 0^+$ state is especially interesting for this method, as it is a 4P-2H state [32]. In the shell-model language, it is an intruder state, because configurations outside the sd-shell are important to get this state right. As the current implementation only includes 3P-1H configuration, this state can provide clues as to what behaviour we can expect from states that are not converged with respect to the level of approximation.
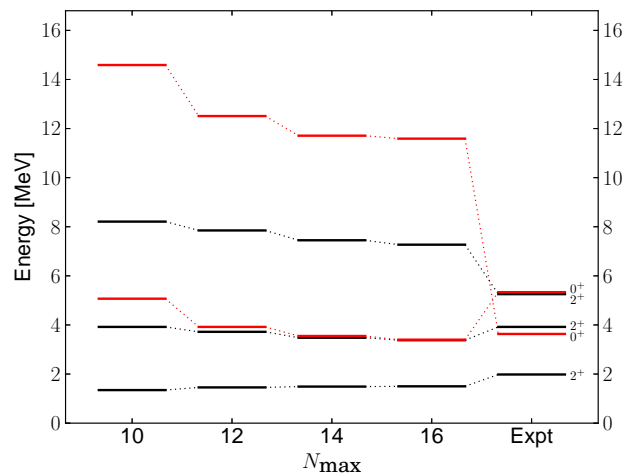

Figure 12: The excitation energies of the first $J^\pi = 1^-$, 2^- and 3^- excited states in ^{18}O for $\hbar\omega = 32$ MeV. The different columns represents different model spaces parametrized by the variable N_{max} (64). The rightmost column contains experimental values from Tilley et al. [31].

Figure 13: The excitation energies of the first few $J^\pi = 0+$ and $2+$ states in ^{18}O for $\hbar\omega = 32$ MeV. The different columns represents different model spaces parametrized by the variable N_{max} (64). The rightmost column contains experimental values from Tilley et al. [31].

In Table VI we list three $J^\pi = 0^+$ states in ^{18}O and none of them stands out. They all have similar partial

State	$n(2p0h)$	Dominant configuration(s)	Weight(s)
$^{18}\text{O}(0_1^+)$	0.69	$(d_{5/2})^2$, $(s_{1/2})^2$	0.52,0.12
$^{18}\text{O}(0_2^+)$	0.69	$(s_{1/2})^2$	0.62
$^{18}\text{O}(0_3^+)$	0.70	$(d_{3/2})^2$	0.62
$^{18}\text{O}(2_1^+)$	0.70	$(d_{5/2})^2$, $(s_{1/2}d_{5/2})$	0.37, 0.27
$^{18}\text{O}(2_2^+)$	0.71	$(s_{1/2}d_{5/2})$, $(d_{5/2})^2$	0.44, 0.26
$^{18}\text{O}(2_3^+)$	0.70	$(d_{5/2})d_{3/2}$, $(s_{1/2}d_{3/2})$	0.49, 0.17
$^{18}\text{O}(3_1^+)$	0.71	$(s_{1/2}d_{5/2})$	0.71
$^{18}\text{O}(4_1^+)$	0.71	$(d_{5/2})^2$	0.64
$^{18}\text{O}(1_1^-)$	0.62	$(p_{3/2}d_{5/2})$,$(p_{3/2}s_{1/2})$, $(d_{5/2}f_{7/2})$	0.22, 0.17, 0.12
$^{18}\text{O}(2_1^-)$	0.65	$(p_{3/2}d_{5/2})$	0.49
$^{18}\text{O}(3_1^-)$	0.62	$(p_{3/2}d_{5/2})$, $(p_{1/2}d_{5/2})$, $(s_{1/2}f_{7/2})$, $(d_{5/2}f_{7/2})$	0.19, 0.12, 0.11, 0.10
$^{18}\text{F}(0_1^+)$	0.69	$(d_{5/2})^2$	0.51
$^{18}\text{F}(1_1^+)$	0.73	$(d_{5/2}d_{3/2})$, $(d_{5/2})^2$, $(s_{1/2})^2$	0.28, 0.22, 0.16
$^{18}\text{F}(2_1^+)$	0.72	$(s_{1/2}d_{5/2})$,$(d_{5/2}d_{3/2})$, $(s_{1/2}d_{3/2})$	0.34, 0.20, 0.14
$^{18}\text{F}(3_1^+)$	0.71	$(s_{1/2}d_{5/2})$, $(d_{5/2})^2$	0.47, 0.18
$^{18}\text{F}(4_1^+)$	0.72	$(d_{5/2})^2$	0.64
$^{18}\text{F}(5_1^+)$	0.72	$(d_{5/2})^2$	0.70

Table VI: This table shows the 2P-0H partial norms(65), as well as the dominant configurations for calculated states in both ^{18}O and ^{18}F. The weights are calculated according to Eq. (67) where all nodes for a given partial wave contribute to the sum.

norms of around 70 percent and are dominated by two neutrons in $d_{5/2}$, $s_{1/2}$ and $d_{3/2}$ respectively. In Fig. 13 we show the convergence patterns for these states, along with those of the three $J^\pi = 2^+$ states. All states show similar level of convergence and it is not possible to single out one of the states. However, if we look at the center-of-mass contamination of these states, the third $J^\pi = 0^+$ shows massive contamination, while the other two show almost none. We therefore chose to associate our $J^\pi = 0^+$ state at 11.6 MeV, with the experimentally observed $J^\pi = 0^+$ state at 3.63 MeV. Our $J^\pi = 0^+$ state at 3.4 MeV is closer in energy, but including effects of three-nucleon forces, pushes this state higher in energy and very close to the experimentally observed $J^\pi = 0^+$ state at 5.34 MeV. [5]. A similar effect occurs among the $J^\pi = 2^+$ excited states, but it is less prominent. Here, the center-of-mass contamination were negliable for all three states.

Let us summarize our discussion of missing many-body correlations. We have identified four different markers to indicate missing phyiscs. Unfortunately, none of them can be used quantitatively and all must be evaluated simultaneously to form a general picture. First, the partial norm can be used to differentiate between different states. From these calculations it seems that a 2P-0H norm of around 70 percent is the standard. A lower partial norm, might indicate the need for 4P-2H correlations. Second, we look at the total weights in the different configurations. If the weights are spread over many different configuartions, as they were in the wave functions of the negative parity states calculated in ^{18}O, this might also indicate missing 4P-2H configurations. Third, we look at the convergence patterns and if energies converge slowly, this probably means that something is missing from the calculation. In weakly bound states for example, continuum effects result in the need for additional resolution in the single particle basis. Finally, we look at the level of center-of-mass contamination present in the wave function. None of these arguments can be analyzed in detail, before 4P-2H configurations are included. We are working on this, but computationally, it will only be possible to include these configurations in a small single particle space. If the 3P-1H and 4P-2H configurations are defined only in a so-called active space around the Fermi level, the computational cost might be manageable. This has been done sucessfully in Gour et al. [33] and should prove to be a valuable approximation also in this method. The formation of a correlated alpha cluster around the Fermi level is important in this mass region and can hopefully be accounted for using a minimal set of 4P-2H configurations.

Let us also look at the convergence of selected states in ^{18}F. In Fig. 14 we show the excitation energy of the first few states in ^{18}F for different model spaces. Here all states are relative well converged, with only the $J^\pi = 4+$ state showing some model space dependence at $N_{\max} = 16$. None of these states have significant center-of-mass contamination and all partial norms are on the same level as can be seen in Table VI. This table also shows that the dominant weights are spread over several different configurations, but all within the sd-shell. According to our earlier discussion, we can find no fault with these states.

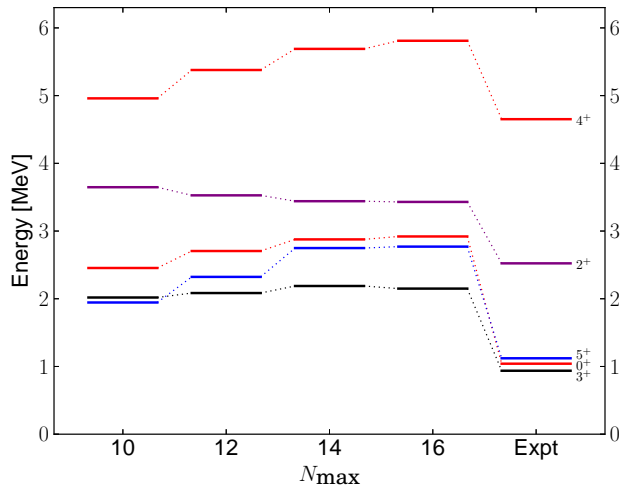In Fig. 15, we plot selected states from the excitation

Figure 14: The excitation energies of the first $J^\pi = 0^+$, 2^+, 3^+, 4^+ and 5^+ states in ^{18}F, calculated at $\hbar\omega = 30$ MeV. The different columns represents different model spaces parametrized by the variable $N_{\max}$ (64). The rightmost column contains experimental values from Tilley et al. [31].
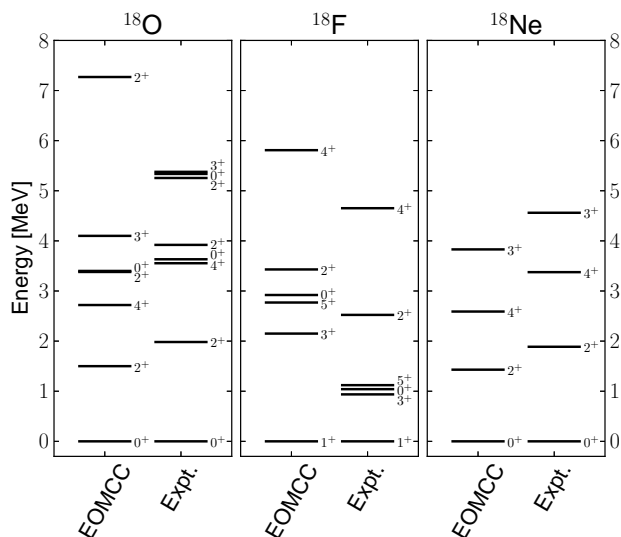

Figure 15: Excitation energies for selected states in ^{18}O, ^{18}F and ^{18}Ne compared to experimental values from Tilley et al. [31].

spectra of ^{18}O, ^{18}F and ^{18}Ne. Only states that are considered good are plotted and compared to their experimental values.

Table VII lists the numerical values, used in Fig. 15 together with the ground state energies for future comparison. The difference in energy between calculations in the two largest model spaces, is listed as the uncertainty of our results in this table. The experimental values are from Tilley et al. [31]

It is clear that the spectrum in ^{18}O and ^{18}Ne is compressed compared to data, while for ^{18}F, the spectra is more open. This is consistent with other calculations us-

^{18}O	Expt.	N^{3}LO ($\Lambda = 500$MeV)
$E_{gs}(0^+)$	-139.807	$-130.00(2)$
$E_{gs}(0_1^+)$	0.0	0.0
$E_x(2_1^+)$	$+1.982$	$+1.50(1)$
$E_x(4_1^+)$	$+3.554$	$+2.72(7)$
$E_x(0_2^+)$	$+3.633$	NA
$E_x(2_2^+)$	$+3.92$	$+3.38(2)$
$E_x(2_3^+)$	$+5.255$	$+7.27(18)$
$E_x(0_3^+)$	$+5.336$	$+3.40(15)$
$E_x(3_1^+)$	$+5.3778$	$+4.12(1)$
^{18}F		
$E_{gs}(1^+)$	-137.370	$-129.75(16)$
$E_{gs}(1^+)$	0.0	0.0
$E_x(3^+)$	$+0.937$	$+2.15(4)$
$E_x(0^+)$	$+1.041$	$+2.92(4)$
$E_x(5^+)$	$+1.121$	$+2.77(2)$
$E_x(2^+)$	$+2.523$	$+3.43(1)$
$E_x(4^+)$	$+4.652$	$+5.81(12)$
^{18}Ne		
$E_{gs}(0^+)$	-132.143	$-122.56(15)$
$E_{gs}(0^+)$	0.0	0.0
$E_x(2^+)$	$+1.887$	$+1.43(3)$
$E_x(4^+)$	$+3.376$	$+2.59(6)$
$E_x(3^+)$	$+4.561$	$+3.83(4)$

Table VII: Results for A=18 systems.

ing different interactions[34–37], where the ^{18}F spectra is much more open compared to experiment than that of ^{18}O. The level ordering is largely reproduced, except for the cases already discussed. A more detailed comparison to experimental data in this region, is difficult to perform before both three-nucleon forces and continuum degrees of freedom are included [5, 38–40].

V. CONCLUSIONS AND OUTLOOK

We have presented the spherical version of the 2PA-EOM-CCSD method, appropriate for the caluclation of energy eigenstates in nuclei that can be described as two particles attatched to a closed (sub-)shell reference. The method has been evaluated in both $A = 6$ and $A = 18$ nuclei, where the results were mostly converged with respect to the single particle basis.

In comparison with a full diagonalization, both ground state and excited state energies were in general very accurate. However, a singular excited state in ^{6}Li deviated significantly from the "exact" result, showing the need to include additional correlations like 4P-2H configurations for the accurate treatment of complex states. For simple states, where a 2P structure is dominant, the current level of truncation is adequate.

In comparison with experiment, both three-nucleon forces and a correct treatment of the scattering con-

tinuum are needed to refine our results.

[1] W. Leidemann and G. Orlandini (2012), submitted to Progress in Particle and Nuclear Physics, nucl-th/1204.4617v1, URL http://arxiv.org/abs/1204.4617v1.

[2] P. Navrátil, S. Quaglioni, I. Stetcu, and B. R. Barrett, Journal of Physics G: Nuclear and Particle Physics **36**, 083101 (2009), URL http://stacks.iop.org/0954-3899/36/i=8/a=083101.

[3] R. J. Bartlett and M. Musiał, Rev. Mod. Phys. **79**, 291 (2007), URL http://link.aps.org/doi/10.1103/RevModPhys.79.291.

[4] I. Shavitt and R. J. Bartlett, *Many-body methods in Chemistry and Physics* (Cambridge University Press, Cambridge, 2009).

[5] G. Hagen, M. Hjorth-Jensen, G. R. Jansen, R. Machleidt, and T. Papenbrock (2012), accepted for publication in Phys. Rev. Lett., nucl-th/1202.2839v1.

[6] G. Hagen, M. Hjorth-Jensen, G. R. Jansen, R. Machleidt, and T. Papenbrock (2012), submitted to PRL, nucl-th/1204.3612v1.

[7] G. R. Jansen, M. Hjorth-Jensen, G. Hagen, and T. Papenbrock, Phys. Rev. C **83**, 054306 (2011), URL http://link.aps.org/doi/10.1103/PhysRevC.83.054306.

[8] G. Hagen, T. Papenbrock, D. J. Dean, and M. Hjorth-Jensen, Phys. Rev. Lett. **101**, 092502 (2008).

[9] G. Hagen, D. J. Dean, M. Hjorth-Jensen, T. Papenbrock, and A. Schwenk, Phys. Rev. C **76**, 044305 (2007).

[10] S. A. Kucharski and R. J. Bartlett, The Journal of Chemical Physics **108**, 5243 (1998), URL http://link.aip.org/link/?JCP/108/5243/1.

[11] A. G. Taube and R. J. Bartlett, The Journal of Chemical Physics **128**, 044110 (pages 13) (2008), URL http://link.aip.org/link/?JCP/128/044110/1.

[12] G. Hagen, T. Papenbrock, D. J. Dean, and M. Hjorth-Jensen, Phys. Rev. C **82**, 034330 (2010).

[13] G. H. Golub and C. F. Van Loan, *Matrix Computations* (Johns Hopkins University Press, Baltimore, 1996).

[14] J. F. Stanton and R. J. Bartlett, J. Chem. Phys. **98**, 7029 (1993).

[15] D. C. Comeau and R. J. Bartlett, Chem. Phys. Letters **207**, 414 (1993).

[16] M. Musiał and R. J. Bartlett, J. Chem. Phys. **119**, 1901 (2003).

[17] M. Musiał, S. A. Kucharski, and R. J. Bartlett, J. Chem. Phys. **118**, 1128 (2003).

[18] G. Hagen, T. Papenbrock, and M. Hjorth-Jensen, Phys. Rev. Lett. **104**, 182501 (2010), URL http://link.aps.org/doi/10.1103/PhysRevLett.104.182501.

[19] A. Bohr and B. R. Mottelson, *Nuclear structure* (Benjamin, New York, 1969).

[20] R. Edmunds, A., *Angular momentum in quantum mechanics* (Princeton university press, Princeton, New Jersey, 1960), 2nd ed.

[21] D. R. Entem and R. Machleidt, Phys. Rev. C **68**, 041001 (2003), URL http://link.aps.org/doi/10.1103/PhysRevC.68.041001.

[22] S. K. Bogner, R. J. Furnstahl, and R. J. Perry, Phys. Rev. C **75**, 061001 (2007), URL http://link.aps.org/doi/10.1103/PhysRevC.75.061001.

[23] G. Hagen, T. Papenbrock, and D. J. Dean, Phys. Rev. Lett. **103**, 062503 (2009), URL http://link.aps.org/doi/10.1103/PhysRevLett.103.062503.

[24] D. Tilley, C. Cheves, J. Godwin, G. Hale, H. Hofmann, J. Kelley, C. Sheu, and H. Weller, Nuclear Physics A **708**, 3 (2002), ISSN 0375-9474, URL http://www.sciencedirect.com/science/article/pii/S03759474020%05973.

[25] P. Navrátil and E. Caurier, Phys. Rev. C **69**, 014311 (2004), URL http://link.aps.org/doi/10.1103/PhysRevC.69.014311.

[26] K. Suzuki and S. Y. Lee, Progress of Theoretical Physics **64**, 2091 (1980), URL http://ptp.ipap.jp/link?PTP/64/2091/.

[27] K. Tsukiyama, S. K. Bogner, and A. Schwenk (2012), nucl-th/1203.2515.

[28] P. Navrátil, V. G. Gueorguiev, J. P. Vary, W. E. Ormand, and A. Nogga, Phys. Rev. Lett. **99**, 042501 (2007), URL http://link.aps.org/doi/10.1103/PhysRevLett.99.042501.

[29] N. Michel, W. Nazarewicz, and M. Płoszajczak, Phys. Rev. C **70**, 064313 (2004), URL http://link.aps.org/doi/10.1103/PhysRevC.70.064313.

[30] G. Hagen, D. J. Dean, M. Hjorth-Jensen, and T. Papenbrock, Phys. Lett. B **656**, 169 (2007).

[31] D. Tilley, H. Weller, C. Cheves, and R. Chasteler, Nuclear Physics A **595**, 1 (1995), ISSN 0375-9474, URL http://www.sciencedirect.com/science/article/pii/037594749500%3381.

[32] P. Ellis and T. Engeland, Nuclear Physics A **144**, 161 (1970), ISSN 0375-9474, URL http://www.sciencedirect.com/science/article/pii/037594747090%4999.

[33] J. R. Gour, P. Piecuch, and M. Włoch, J. Chem. Phys. **123**, 134113 (2005).

[34] M. F. Jiang, R. Machleidt, D. B. Stout, and T. T. S. Kuo, Phys. Rev. C **46**, 910 (1992), URL http://link.aps.org/doi/10.1103/PhysRevC.46.910.

[35] X.-W. Pan, T. Kuo, M. Vallières, D. H. Feng, and A. Novoselsky, Physics Reports **264**, 311 (1996), ISSN 0370-1573, URL http://www.sciencedirect.com/science/article/pii/037015739500%0453.

[36] J. D. Holt, J. W. Holt, T. T. S. Kuo, G. E. Brown, and S. K. Bogner, Phys. Rev. C **72**, 041304 (2005), URL http://link.aps.org/doi/10.1103/PhysRevC.72.041304.

[37] H. Dong, T. T. S. Kuo, and J. W. Holt (2011), to be submitted, nucl-th/1105.4169v1, URL http://arxiv.org/abs/1105.4169v1.

[38] A. Volya and V. Zelevinsky, Phys. Rev. Lett. **94**, 052501 (2005), URL http://link.aps.org/doi/10.1103/PhysRevLett.94.052501.

[39] G. Hagen, T. Papenbrock, D. J. Dean, M. Hjorth-Jensen, and B. V. Asokan, Phys. Rev. C **80**, 021306 (2009).

[40] T. Otsuka, T. Suzuki, J. D. Holt, A. Schwenk, and Y. Akaishi, Phys. Rev. Lett. **105**, 032501 (2010), URL http://link.aps.org/doi/10.1103/PhysRevLett.105.

032501.

Appendix A: REDUCED MATRIX ELEMENTS

The reduced matrix elements of a spherical tensor operator $\hat{T}_M^J$ of rank J and projection M, are defined according to the Wigner-Eckart theorem,

$$\langle \alpha; J_\alpha M_\alpha | \hat{T}_M^J | \beta; J_\beta M_\beta \rangle = C_{MM_\beta M_\alpha}^{JJ_\beta J_\alpha} \langle \alpha; J_\alpha || \hat{T}^J || \beta; J_\beta \rangle. \tag{A1}$$

Here, α and β are general labels representing all quantum numbers except angular momentum and its projection, while $J_\alpha(M_\alpha)$ and $J_\beta(M_\beta)$ are the total angular momentum(projection) of the bra and ket state respectively. The double bars denote reduced matrix elements and does not depend on any of the angular momentum projections and $C_{MM_\beta M_\alpha}^{JJ_\beta J_\alpha}$ is a Clebsch-Gordon coefficient.

In coupled-cluster, the unknown amplitudes are the matrix elements of the cluster operator $\hat{T}_0^0$

$$t_i^a = \langle a; j_a m_a | \hat{T}_0^0 | i; j_i m_i \rangle$$
$$t_{ij}^{ab} = \langle ab; j_a m_a j_b m_b | \hat{T}_0^0 | ij; j_i m_i j_j m_j \rangle$$
$$\vdots = \vdots,$$

where the operator sub- and superscript identifies the cluster operator as a scalar under rotation. Also, the labels $abij\dots$, denote single particle states and we have singled out the angular momentum(projection) in the labels $j_a(m_a)$ etc.

Now, the reduced matrix elements of the cluster operator are defined according to Eq. (A1). For example,

$$\langle ab; j_a m_a j_b m_b | \hat{T}_0^0 | ij; j_i m_i j_j m_j \rangle =$$
$$\sum_{\substack{J_{ab} M_{ab} \\ J_{ij} M_{ij}}} C_{m_a m_b M_{ab}}^{j_a j_b J_{ab}} C_{m_i m_j M_{ij}}^{j_i j_j J_{ij}} C_{0 M_{ij} M_{ab}}^{0 J_{ij} J_{ab}}$$
$$\times \langle ab; j_a j_b; J_{ab} || \hat{T}^0 || ij; j_i j_j; J_{ij} \rangle,$$

where the sum and the first two Clebsch-Gordon coefficients come from the coupling of j_a and j_b to J_{ab} and of j_i and j_j to J_{ij}, in that specific order This expression is simplified by the explicit evaluation of the third Clebsch-Gordon coefficient

$$C_{0 M_{ij} M_{ab}}^{0 J_{ij} J_{ab}} = \delta_{J_{ab}, J_{ij}=J} \delta_{M_{ab}, M_{ij}=M},$$

where $\delta_{\alpha, \beta}$ is the Kronecker delta. We get

$$\langle ab; j_a m_a j_b m_b | \hat{T}_0^0 | ij; j_i m_i j_j m_j \rangle =$$
$$\sum_{JM} C_{m_a m_b M}^{j_a j_b J} C_{m_i m_j M}^{j_i j_j J} \langle ab; j_a j_b; J || \hat{T}^0 || ij; j_i j_j; J \rangle.$$

When this specific coupling order is used(left to right) and no confusion will arise, we will use a shorthand notation for the reduced matrix elements, defined by

$$t_i^a(J) = \langle a; J || \hat{T}^0 || i; J \rangle \tag{A2}$$
$$t_{ij}^{ab}(J) = \langle ab; j_a j_b; J || \hat{T}^0 || ij; j_i j_j; J \rangle. \tag{A3}$$

The transformations between the reduced amplitudes and the original amplitudes of the cluster operator are defined as

$$t_i^a(J) = \delta_{j_a, j_i=J} t_i^a \tag{A4}$$
$$t_i^a = \delta_{j_a, j_i=J} t_i^a(J) \tag{A5}$$
$$t_{ij}^{ab}(J) = \frac{1}{\hat{J}^2} \sum_{\substack{m_a m_b \\ m_i m_j M}} C_{m_a m_b M}^{j_a j_b J} C_{m_i m_j M}^{j_i j_j J} t_{ij}^{ab} \tag{A6}$$
$$t_{ij}^{ab} = \sum_{JM} C_{m_a m_b M}^{j_a j_b J} C_{m_i m_j M}^{j_i j_j J} t_{ij}^{ab}(J), \tag{A7}$$

where we use the convention $\hat{J} = \sqrt{2J+1}$.

As the similarity transformed Hamiltonian($\bar{H}$) is a scalar under rotation as well, the shorthand form of its reduced matrix elements are defined analogously

$$\bar{H}_q^p(J) = \langle p; J || \bar{H}^0 || q; J \rangle \tag{A8}$$
$$\bar{H}_{rs}^{pq}(J) = \langle pq; j_p j_q; J || \bar{H}^0 || rs; j_r j_s; J \rangle. \tag{A9}$$

The transformations between the original and reduced matrix elements are given by

$$\bar{H}_q^p(J) = \delta_{j_p, j_q=J} \bar{H}_q^p \tag{A10}$$
$$\bar{H}_q^p = \delta_{j_p, j_q=J} \bar{H}_q^p(J) \tag{A11}$$
$$\bar{H}_{rs}^{pq}(J) = \frac{1}{\hat{J}^2} \sum_{\substack{m_p m_q \\ m_r m_s M}} C_{m_p m_q M}^{s_p s_q J} C_{m_r m_s M}^{s_r s_s J} \bar{H}_{rs}^{pq} \tag{A12}$$
$$\bar{H}_{rs}^{pq} = \sum_{JM} C_{m_p m_q M}^{s_p s_q J} C_{m_r m_s M}^{s_r s_s J} \bar{H}_{rs}^{pq}(J). \tag{A13}$$

The original matrix elements of the similarity transformed Hamiltonian are defined in Jansen et al. [7].

The r-amplitudes are the matrix elements of the excitation operator in Eq. (46)

$$r^{ab} = \langle ab; j_a m_a j_b m_b | \hat{R}_M^J | 0 \rangle$$
$$r_i^{abc} = \langle abc; j_a m_a j_b m_b j_c m_c | \hat{R}_M^J | i; j_i m_i \rangle,$$

where the operator is now a general tensor operator of rank J and projection M. The bra side contains up to three indices and we have to couple three angular momentum vectors to be able to define the reduced amplitudes. Using r_i^{abc} as an example, we couple from left to right and get

$$\langle abc; j_a m_a j_b m_b j_c m_c | \hat{R}_M^J | i; j_i m_i \rangle =$$
$$\sum_{\substack{J_{ab} M_{ab} \\ J_{abc} M_{abc}}} C_{m_a m_b M_{ab}}^{j_a j_b J_{ab}} C_{M_{ab} m_c M_{abc}}^{J_{ab} j_c J_{abc}} C_{M m_i M_{abc}}^{J j_i J_{abc}}$$
$$\langle abc; j_a j_b; J_{ab} j_c; J_{abc} || \hat{R}^J || i; j_i \rangle,$$

where the last Clebsch-Gordon coefficient is due to the Wigner-Eckart theorem. We let the order of the angular momentum labels on the bra-side specify the coupling order, where j_a and j_b couples to J_{ab}. In turn, J_{ab} and j_c

couples to J_{abc}. When this coupling order has been used and no confusion will arise, we will use the shorthand notation for the reduced elements, defined by

$$r^{ab}(J) = \langle ab; j_a j_b; J || \hat{R}^J || o \rangle \quad \text{(A14)}$$

$$r_i^{abc}(J, J_{abc}, J_{ab}) = \langle abc; j_a j_b; J_{ab} j_c; J_{abc} || \hat{R}^J || i; j_i \rangle. \quad \text{(A15)}$$

In the shorthand notation, the transformations between the reduced and the original amplitudes is

$$r^{ab}(J) = \frac{1}{\hat{J}^2} \sum_{M m_a m_b} r^{ab} C_{m_a m_b M}^{j_a j_b J} \quad \text{(A16)}$$

$$r^{ab} = C_{m_a m_b M}^{j_a j_b J} r^{ab}(J) \quad \text{(A17)}$$

$$r_i^{abc}(J, J_{abc}, J_{ab}) = \frac{1}{\hat{J}_{abc}^2} \sum_{\substack{M M_{abc} M_{ab} \\ m_a m_b m_c m_i}} r_i^{abc} C_{m_a m_b M_{ab}}^{j_a j_b J_{ab}}$$
$$\times C_{M_{ab} m_c M_{abc}}^{J_{ab} j_c J_{abc}} C_{M m_i M_{abc}}^{J j_i J_{abc}}. \quad \text{(A18)}$$

$$r_i^{abc} = \sum_{\substack{J_{abc} M_{abc} \\ J_{ab} M_{ab}}} r_i^{abc}(J, J_{abc}, J_{ab})$$
$$\times C_{m_a m_b M_{ab}}^{j_a j_b M_{ab}} C_{M_{ab} m_c M_{abc}}^{J_{ab} j_c J_{abc}} C_{M m_i M_{abc}}^{J j_i J_{abc}}. \quad \text{(A19)}$$

Appendix B: PERMUTATION OPERATORS

The diagrams in Table I contain permutation operators that guarantees an antisymmetric final wave function. In the uncoupled formalism, these were simple and defined by

$$\hat{P}(ab) = \hat{1} - \hat{P}_{a,b} \quad \text{(B1)}$$

$$\hat{P}(ab, c) = \hat{1} - \hat{P}_{a,c} - \hat{P}_{b,c}, \quad \text{(B2)}$$

where $\hat{P}_{a,b}$ permutes indices a and b and $\hat{1}$ is the identity operator. In the spherical formalism, this simple form is not adequate, as a specific coupling order is used in all reduced amplitudes. To see why, let us apply $\hat{P}_{a,b}$ to a reduced amplitude $r^{ab}(J)$

$$\hat{P}_{a,b} \langle ab; j_a j_b; J || \hat{R}^J || 0 \rangle = \langle ba; j_a j_b; J || \hat{R}^J || 0 \rangle$$

While this coupling order is the correct order when calculating the contribution to $\left(\bar{H}\hat{R}\right)^{ab}$, the reduced amplitudes are defined in a different coupling order. To compensate, we change the coupling order and introduce a phase(See Edmunds [20] for details)

$$|ba; j_a j_b; J\rangle = (-1)^{j_a + j_b - J} |ba; j_b j_a; J\rangle.$$

Thus, we define

$$\hat{P}(ab) = \hat{1} - (-1)^{j_a + j_b - J} \hat{P}_{a,b}, \quad \text{(B3)}$$

and applied to the reduced amplitude $r^{ab}(J)$ this has the correct form

$$\hat{P}(ab) r^{ab}(J) = r^{ab}(J) - (-1)^{j_a + j_b - J} r^{ba}(J).$$

The permutation operators $\hat{P}_{a,c}$ and $\hat{P}_{b,c}$ in Eq. (B2) are a bit more complicated, as they involve three particle states. We use standard expressions for coupling three angular momentum

$$|cba; j_a j_b; J_{ab} j_c; J_{abc} M_{abc}\rangle = -\sum_{J_{cb}} \hat{J}_{cb} \hat{J}_{ab} \begin{Bmatrix} j_c & j_b & J_{cb} \\ j_a & J_{abc} & J_{ab} \end{Bmatrix}$$
$$\times |cba; j_c j_b; J_{cb} j_a; J_{abc} M_{abc}\rangle$$

$$|acb; j_a j_b; J_{ab} j_c; J_{abc} M_{abc}\rangle = \sum_{J_{ac}} (-1)^{j_b + j_c - J_{ab} + J_{ac}} \hat{J}_{ab} \hat{J}_{ac}$$
$$\times \begin{Bmatrix} j_c & j_a & J_{ac} \\ j_b & J_{abc} & J_{ab} \end{Bmatrix}$$
$$\times |acb; j_a j_c; J_{ac} j_b; J_{abc} M_{abc}\rangle$$

Thus, we define

$$\hat{P}(ab, c) = \hat{1} + \sum_{J_{cb}} \hat{J}_{cb} \hat{J}_{ab} \begin{Bmatrix} j_c & j_b & J_{cb} \\ j_a & J_{abc} & J_{ab} \end{Bmatrix} \hat{P}_{a,c} -$$
$$\sum_{J_{ac}} (-1)^{j_b + j_c - J_{ab} + J_{ac}} \hat{J}_{ab} \hat{J}_{ac} \times \begin{Bmatrix} j_c & j_a & J_{ac} \\ j_b & J_{abc} & J_{ab} \end{Bmatrix} \hat{P}_{b,c}, \quad \text{(B4)}$$

Since this anti symmetrization contributes a significant part of the overall calculation, all diagrams containing this operator is applied only once to the sum of all diagrams containing this operator.

Appendix C: THREE-BODY PARTS OF $\bar{H}$

There are two three-body matrix elements of $\bar{H}$ that contributes to the 3P-1H amplitudes. But since the original Hamiltonian does not contain three-body elements, these deserve special attention. These elements can be factorized in just the same way as the coupled-cluster amplitude equations, to reduce the computational cost of these diagrams. The two three-body contributions to the 3P-1H amplitudes are

$$(\bar{H}\hat{R})_i^{abc} \leftarrow \frac{1}{2} \bar{H}_{efi}^{abc} r^{ef} + \frac{1}{2} P(a, bc) \bar{H}_{efi}^{bmc} r_m^{aef}$$
$$= -\frac{1}{2} P(a, bc) \bar{H}_{ef}^{am} r^{ef} t_{mi}^{bc} + \frac{1}{2} P(a, bc) \bar{H}_{ef}^{mn} r^{ef} t_{ni}^{bc} t_m^a$$
$$+ \frac{1}{2} P(a, bc) \bar{H}_{ef}^{mn} t_{ni}^{bc} r_m^{aef}.$$

These terms are factorized to get

$$(\bar{H}\hat{R})_i^{abc} \leftarrow \frac{1}{2} P(a, bc) t_{im}^{ab} \chi_m^c$$

where we have defined the intermediate

$$\chi_m^c = \bar{H}_{ef}^{cm} r^{ef} + \bar{H}_{ef}^{mn} t_n^c + r_n^{efc}. \quad \text{(C1)}$$

Note that we have swapped the indices to facilitate the angular momentum coupling. Now the angular momentum coupling in the coupled-cluster amplitudes match the coupling in the 3P-1H amplitudes, so we do not need to break these couplings when rewriting the diagram in a spherical basis.

In the spherical formulation, it is clear that χ_m^c are the reduced matrix elements of the tensor operator $\hat{\chi}^J$, which has the same rank as $\hat{R}^J$. This is a consequence of the scalar character of $\bar{H}$. By coupling the matrix elements in Eq. (C1) to form reduced matrix elements, we get the following expression for the reduced matrix elements of $\hat{\chi}^J$

$$\chi_m^c(J) = -r^{ef}(J)\bar{H}_{ef}^{mc}(J) + r^{ef}(J)\bar{H}_{ef}^{mn}(J)t_n^c$$

$$+ \sum_{J_{ef},J_{efc}} (-1)^{j_c+j_m+J_{ef}-J} \frac{\hat{J}\hat{J}_{ef}}{\hat{j}_{efc}^2} \begin{Bmatrix} j_c & j_m & J \\ j_m & J_{efc} & J_{ef} \end{Bmatrix}$$

$$\times r_n^{efc}(J_{ef},J_{efc},J)\bar{H}_{ef}^{mn}(J_{ef}). \quad (C2)$$